

**NTHMP Current Benchmark Workshop:
FUNWAVE–TVD results**

Research Report No. CACR-16-01

James T. Kirby¹, Fengyan Shi¹, Stephan Grilli²
Fatemeh Nemati², Babak Tehranirad¹

¹Center for Applied Coastal Research,
Department of Civil and Environmental Engineering,
University of Delaware, Newark, DE 19716 USA

²Department of Ocean Engineering
University of Rhode Island
Narragansett, RI 02882 USA

Supported by the National Tsunami Hazard Mitigation Program
National Weather Service Grant NA14NWS4670041

April 12, 2017

Abstract

This report describes benchmark testing of the Boussinesq model FUNWAVE-TVD. The work was carried out in conjunction with the National Tsunami Hazard Mitigation Program's Workshop on Modeling of Tsunami Currents, held in Portland, Oregon on March 9-10, 2015. A website describing the workshop may be found at http://coastal.usc.edu/currents_workshop/. This report describes results obtained for all five proposed benchmarks described on the site.

Contents

1	Introduction	1
2	Model Background	2
3	Model Equations	3
4	Numerical Solution Method	4
5	Benchmark Problem Comparisons	5
5.1	Steady flow over a submerged obstacle	6
5.1.1	Model configuration	8
5.1.2	Numerical results	8
5.2	Tsunami currents in Hilo Harbor	11
5.2.1	Numerical model configuration	13
5.2.2	Local simulations	17
5.2.3	Global simulations	24
5.3	Tsunami currents in Tauranga Harbor	31
5.3.1	Introduction	31
5.3.2	Definition of FUNWAVE-TVD model grids	32
5.3.3	Results: Tsunami simulations	36
5.3.4	Results: Tide simulations	40
5.3.5	Results: Tide plus tsunami simulations	42
5.4	Benchmark Test 4: Seaside, Oregon	44

5.4.1	Model Setup	49
5.4.2	Results	52
5.4.3	Convergence	53
5.4.4	The effect of bathymetry smoothing	55
5.5	Solitary Wave Propagation over a Complex Shelf	61

List of Figures

1	Geometry of experiments of Lloyd and Stansby (1997a,b).	7
2	Experimental data (dots) and numerical simulation (solid line, not shown) for a) u velocity component at time series location 1, b) v velocity component at time series location 1, c) u velocity component at time series location 2, and d) v velocity component at time series location 2.	10
3	Footprint of Hilo Harbor computational grids G4 (20 m), G5 (10 m), G6 (5 m) (Table 2) with location of control point (CP), tide gage (TG), ADCPs (ADCP1, ADCP2), and Near Hilo Harbor Station (NHHS) (Table 1).	12
4	Footprints of nested computational grids G0 to G3 (Table 2). Color scale is bathymetry (< 0) and topography (> 0) of grid G0 in meter.	13
5	Footprints of nested computational grids G1 to G4 (Table 2). Color scale is bathymetry (< 0) and topography (> 0) of grid G1 in meter. Location of dart buoy #51407 is marked.	15
6	Footprints of nested computational grids G2 to G4 (Table 2). Color scale is bathymetry (< 0) and topography (> 0) of grid G2 in meter. Location of dart buoy #51407 is marked.	16
7	<i>Local simulations.</i> Comparison of time series of surface elevation computed in grids G4 (green), G5 (red) and G6 (blue) at the Control Point Station (CP; Fig. 6, Table 1), with each other and with the benchmark data (black).	19

8 *Local simulations.* Comparison of time series of surface elevation computed in grids G4 (green), G5 (red) and G6 (blue) at the Tide Gage Station (TG; Fig. 6, Table 1), with each other and with field data (black with (●) symbols). 20

9 *Local simulations.* Comparison of time series of horizontal current (U, V) computed in grids G4 (green), G5 (red) and G6 (blue) at the ADCP1 Station (Fig. 6, Table 1), with each other and with field data (black with (●) symbols). 20

10 *Local simulations.* Comparison of time series of horizontal current (U, V) computed in grids G4 (green), G5 (red) and G6 (blue) at the ADCP2 Station (Fig. 6, Table 1), with each other and with field data (black with (●) symbols). 21

11 *Local simulations.* Comparison of time series of horizontal current magnitude computed in grids G4 (green), G5 (red) and G6 (blue) at the ADCP1 Station (Fig. 6, Table 1), with each other and with field data (black with (●) symbols). 21

12 *Local simulations.* Comparison of time series of horizontal current magnitude computed in grids G4 (green), G5 (red) and G6 (blue) at the ADCP2 Station (Fig. 6, Table 1), with each other and with field data (black with (●) symbols). 22

13	<i>Local simulations.</i> Envelopes of maximum horizontal current magnitude computed for the entire simulations in grids : (a) G4 (20 m), (b) G5 (10 m) and (c) G6 (5 m). Note that axes are numbered with the Cartesian grid cell indices.	23
14	Source of the Mw 9.1 Tohoku 2011 event computed with NHWAVE at 300 s after the earthquake (Grilli et al. 2013; Tappin et al., 2014): (a) sea surface elevation (m); and (b) horizontal velocity magnitude (m/s). Note the long-crested seismic waves generated to the south by the earthquake and the shorter-dispersive cylindrical waves generated to the north by the secondary SMF mechanism.	24
15	<i>Global simulations.</i> Comparison of time series of surface elevation computed in grids G0 (blue), G1 (green) and G2 (red) at Dart buoy #51407 (Fig. 6; Table 1), with each other and with field data (black). Note, results in grid G1 and G2 are indistinguishable. Numerical data is shifted 2 min backwards.	27
16	<i>Global simulations.</i> Comparison of time series of surface elevation computed in grids G4 (green), G5 (red) and G6 (blue) at the Near Hilo Harbor Station (NHHS; Fig. 3, Table 1), with each other.	27
17	<i>Global simulations.</i> Comparison of time series of surface elevation computed in grids G4 (green), G5 (red) and G6 (blue) at the Control Point Station (CP; Fig. 3, Table 1), with each other and with field data (black). (simulation time was shifted by 5.8 min to improve phase match)	28

18	<p><i>Global simulations.</i> Comparison of time series of surface elevation computed in grids G4 (green), G5 (red) and G6 (blue) at the Tide Gage Station (TG; Fig. ??, Table 1), with each other and with field data (black with (●) symbols). (simulation time was shifted by 5.8 min to improve phase match)</p>	28
19	<p><i>Global simulations.</i> Comparison of time series of horizontal current (U, V) computed in grids G4 (green), G5 (red) and G6 (blue) at the ADCP1 Station (Fig. 3, Table 1), with each other and with field data (black with (●) symbols). (simulation time was shifted by 5.8 min to improve phase match)</p>	29
20	<p><i>Global simulations.</i> Comparison of time series of horizontal current (U, V) computed in grids G4 (green), G5 (red) and G6 (blue) at the ADCP2 Station (Fig. 3, Table 1), with each other and with field data (black with (●) symbols). (simulation time was shifted by 5.8 min to improve phase match)</p>	30
21	<p>Shore-oriented (x) bathy/topo (color scale in m) of 40 m Cartesian FUNWAVE-TVD grid, with a 10 m nested Cartesian grid (black box). Locations of measuring equipment are shown as red dots. Tide stations are marked as follows: (1) A Beacon, (2) Tug Berth, (3) Sulfur Point and (4) Moturiki. An ADCP buoy is anchored in the middle of the inlet (slack mooring) at dot marked (5). A-Beacon provides the inflow boundary conditions along the upper offshore boundary.</p>	34

22	Zoom-in of (a,c) 40 meter; and (b,d) 10 m resolution Cartesian grids (axes are numbered by cell numbers), without and with an obstacle boundary. The obstacles (no-flux boundary condition shaded in black) were inserted in place of the steep bathymetry at the shore, near the stations marked (2) and (3). The location of data comparison points are indicated with red marks. From left to right, these points are: (5) ADCP Buoy, (4) Moturiki, (2) Tug Berth, and (3) Sulfur Point. A Beacon is located to the northeast.	35
23	(a) Tsunami only simulations: initial discrepancy between specified surface elevation at A Beacon (black solid line), based on tsunami observations, and surface elevations computed with FUNWAVE-TVD (chained line); converged boundary condition (blue solid line line). (b) Tide only simulation: tide data at A Beacon (black solid line); OTPS model prediction (chained line); and the same corrected by 4% (blue solid line) used as a boundary condition. (c) Tsunami plus tide simulation: combined surface elevation specified as a boundary condition (black solid line) at A Beacon, compared to values computed in FUNWAVE-TVD (blue solid line).	37
24	Tsunami only simulations: convergence of boundary condition for the input velocity module, (a) $ U $ and components (b) u and (c) v , at A Beacon, in successive simulations in FUNWAVE-TVDs 40 m grid offshore boundary. Initial input velocity, based on a linear long wave approximation (black solid line), successive computations (dashed line), and the final input boundary condition (blue solid line).	38

25	Tsunami only simulations. Measured tsunami surface elevations (solid line), detided and compared to FUNWAVE-TVDs 40 meter grid results (dashed line) and 10 meter grid results (blue solid line), at four locations: (a) A Beacon, (b) Tug Berth, (c) Sulfur Point, (d) Moturiki.	39
26	Tide only simulations. Measured tide surface elevations (solid line), compared to FUNWAVE-TVDs 40 meter grid results (dashed line) and 10 meter grid results (blue solid line), at four locations: (a) A Beacon, (b) Tug Berth, (c) Sulfur Point, (d) Moturiki.	41
27	Tide-tsunami simulations. Measured surface elevations (solid line), compared to FUNWAVE-TVDs 40 meter grid results of tide and tsunami alone linearly superimposed (dashed line) and results of simulations using a combined tide-tsunami boundary condition (blue solid line), at three locations: (a) A Beacon, (b) Tug Berth, (c) Sulfur Point.	43
28	Surface elevations predicted by FUNWAVE-TVD in the 40 meter (solid blue line) and 10 meter (black dashed line) grid, at the ADCP buoy location (Fig. 21), in: (a) tide only, (b) tsunami only; and (c) tide-tsunami simulations. The shaded region represents the range of surface elevations predicted within the buoy 40 m radius of giration.	45

29	Tsunami only simulations. Measured tsunami current magnitude $ U $ and velocity components, u and v at the ADCP buoy (solid line), detided and compared to FUNWAVE-TVDs 40 meter grid results (dashed line) and 10 meter grid results (blue solid line). The shaded region represents the range of values predicted in the 10 m grid, within the buoy 40 m radius of giration.	46
30	Tide only simulations. Measured tide current magnitude $ U $ and velocity components, u and v at the ADCP buoy (solid line), compared to FUNWAVE-TVDs 40 meter grid results (dashed line) and 10 meter grid results (blue solid line). The shaded region represents the range of values predicted in the 10 m grid, within the buoy 40 m radius of giration.	47
31	The complete velocity signal (tide and tsunami) measured at the ADCP buoy are represented with the solid line. The dashed line indicates FUNWAVE-TVD output at the anchor point location, and the shaded region indicates the maximum and minimum values within 40 meters of the anchor point. The magnitude of the velocity is shown in (a). The u and v components of the velocity are aligned with the orientation of the simulation grids, and are shown in (b) and (c). Time is measured in hours after the earthquake.	48
32	The Bathymetry Data.	49
33	Location of gauges.	50
34	Water surface in the left part of the domain obtained from recorded data. .	52
35	Comparison between 5 different friction values for B1.	53
36	Comparison between 5 different friction values for B4.	54

37	Comparison between 5 different friction values for B6.	54
38	Comparison between 5 different friction values for B9.	55
39	Comparison between calculated cross-shore velocity for 5 different grid sizes at B1.	56
40	Difference plot between the smoothed and original bathymetry close to the U-shape structure next to B1 and B4.	57
41	The figure on the left shows the original onshore bathymetry used in runs 1-9, and the figure on the left shows the smoothed bathymetry used in run 10.	58
42	Comparison between original and smoothed bathymetry for B1.	59
43	Comparison between original and smoothed bathymetry for B4.	59
44	Comparison between original and smoothed bathymetry for B6.	60
45	Comparison between original and smoothed bathymetry for B9.	60
46	Basin geometry and gauge locations. Experiment of Swigler (2009).	62
47	Simulated solitary wave run-up on model bathymetry (after Shi et al., 2012).	63
48	Model/data comparisons of time series of surface elevation at Gauge 1-Gauge9 (from top to bottom). Solid line: data, red dashed line: VIS breaker model, blue dashed line: SWE breaker model.	64
49	Model/data comparisons of time series of velocity components (u,v) at ADV 1. Solid line: data, red dashed line: VIS breaker model, blue dashed line: SWE breaker model.	65

List of Tables

- 1 Definition and location of numerical wave gages used in FUNWAVE-TVD simulations. 11
- 2 Parameters of numerical grids used in FUNWAVE-TVD simulations (GMRT data was obtained from <http://www.marine-geo.org/tools/GMRTMapTool>) 14
- 3 Different runs performed for this benchmark. 51

1 Introduction

This report describes benchmark testing of the Boussinesq model FUNWAVE-TVD. The work was carried out in conjunction with the National Tsunami Hazard Mitigation Program's Workshop on Modeling of Tsunami Currents, held in Portland, Oregon on March 9-10, 2015. A website describing the workshop may be found at http://coastal.usc.edu/currents_workshop/. This report describes results obtained for all five proposed benchmarks described on the site, including:

1. A laboratory study on a shallow wake behind a submerged conical seamount (Lloyd and Stansby, 1999)
2. Tsunami currents in Hilo Harbor, HI during the 2011 Tohoku-oki event (Cheung et al, 2013).
3. Combined tidal and tsunami elevations and currents in Tauranga Harbor, NZ during the Tohoku event. (Borrero, et al, 2012)
4. Laboratory experiment on inundation of a model of Seaside, OR by a solitary-like wave (Park et al., 2013)
5. Laboratory experiment on solitary wave runup on a complex shelf (Switzer and Lynett, XXX)

A description of numerical results for all teams taking part in the benchmarking exercise may be found in Lynett et al (2016). The results of the workshop are summarized in Lynett et al (2017).

2 Model Background

FUNWAVE-TVD is the present stage of evolution of a depth-integrated, fully nonlinear Boussinesq model originally proposed in Wei et al. (1995). The development of the original finite difference form of the model is described by Kennedy et al. (2000) and Chen et al. (2000), and the was distributed to the user community as open source code in this form for over a decade, with an extensive list of publications resulting from its worldwide use. The model was extensively rewritten in 2010-2011 using a finite volume TVD scheme in order to take advantage of the stability properties and shock-capturing capabilities of the approach, and to utilize Riemann solvers to improve wetting-drying processes during inundation. The work described here uses a version of the code developed for a Cartesian coordinate system, described by Shi et al. (2012) as well as a corresponding version in spherical polar coordinates for use in ocean scale propagation, described by Kirby et al. (2013).

FUNWAVE-TVD has been used for all propagation and inundation modeling in NTHMP work for the US East Coast. Descriptions of the early stages of this work may be found in Abadie et al. (2012), Grilli et al. (2015) and Tehranirad et al. (2015). The model was previously benchmarked for inundation during the original NTHMP benchmark workshop; detailed results are provided in Tehranirad et al. (2011).

3 Model Equations

Various versions of BTM models exist in the literature. A representative example retaining terms to $O(\mu^2)$ may be written as a two equation system for surface displacement η and a horizontal velocity at a reference depth, $\mathbf{u}_\alpha = \mathbf{u}(z_\alpha)$ (Nwogu, 1993) given by (Chen, 2006; Shi et al., 2012)

$$\eta_t + \nabla_h \cdot \mathbf{M} = 0 \quad (1)$$

$$\mathbf{u}_{\alpha,t} + \delta \mathbf{u}_\alpha \cdot \nabla_h \mathbf{u}_\alpha + \nabla_h \eta + \mu^2 (\mathbf{V}_1 + \mathbf{V}_2 + \overline{\mathbf{V}}_3) + \mathbf{R} = O(\mu^4) \quad (2)$$

where \mathbf{M} is depth-integrated volume flux or momentum, and where

$$\begin{aligned} \mathbf{V}_1 &= \left[\frac{z_\alpha^2}{2} \nabla_h B + z_\alpha \nabla_h A \right]_{,t} - \nabla_h \left[\frac{\eta^2}{2} B_t + \eta A_t \right] \\ \mathbf{V}_2 &= \nabla_h \left[(z_\alpha - \eta) (\mathbf{u}_\alpha \cdot \nabla_h) A + \frac{1}{2} (z_\alpha^2 - \eta^2) (\mathbf{u}_\alpha \cdot \nabla_h) B + \frac{1}{2} (A + \eta B)^2 \right] \\ \overline{\mathbf{V}}_3 &= \Omega_0 \mathbf{i}_z \times \overline{\mathbf{u}}_2 + \Omega_2 \mathbf{i}_z \times \mathbf{u}_\alpha \end{aligned} \quad (3)$$

with

$$A = \nabla_h \cdot (h \mathbf{u}_\alpha); \quad B = \nabla_h \cdot \mathbf{u}_\alpha \quad (4)$$

Vertical structure of the horizontal velocity is given by

$$\mathbf{u}_2(z) = (z_\alpha - z) \nabla_h A + \frac{1}{2} (z_\alpha^2 - z^2) \nabla_h B \quad (5)$$

and is determined by imposing zero horizontal vorticity. Ω_0, Ω_2 denote the magnitudes of vertical vorticity vectors corresponding the curl of velocities $\mathbf{u}_\alpha, \mathbf{u}_2$ respectively.

In (2), R represents diffusive and dissipative terms including bottom friction, subgrid turbulent mixing and breaking induced dissipation if the artificial eddy viscosity breaking scheme (Kennedy et al., 2000) is applied. A quadratic form of bottom friction written in terms of a spatially varying drag coefficient C_d was used as. For modeling of wave breaking, two options were implemented in the model. One is the natural TVD shock capturing scheme which switches the Boussinesq equations to the nonlinear shallow water equations at cells where the ratio of surface elevation to water depth exceeds a certain threshold (SWE breaker, Tonelli and Petti, 2009, 2010). The other is the artificial eddy-viscosity breaker (VIS breaker) developed by Kennedy et al. (2000).

For solution the equations are re-written in quasi-conservative form and solved using a second-order MUSCL-TVD finite volume scheme, Details may be found in Shi et al. (2012). A version of the code in spherical polar coordinates, used for Pacific Ocean - scale propagation in Benchmark 2 (Section 5.2) is given by Kirby et al. (2013).

4 Numerical Solution Method

In FUNWAVE-TVD, a combined finite-volume and finite-difference method is applied to the spatial discretization. For the flux terms and the first-order derivative terms, a high-order MUSCL-TVD scheme is used. The MUSCL-TVD scheme implemented in the model includes different orders of accuracy from second- to fourth-order (Yamamoto et al., 1993, 1998), which can be chosen by a user. The van-Leer limiter is used for the third-

order and the second-order schemes and the Minmod limiter is used for the fourth-order scheme. The numerical fluxes are computed using a HLL approximate Riemann solver. For time stepping, the third-order Strong Stability-Preserving (SSP) Runge-Kutta scheme (Gottlieb et al., 2001) is adopted. An adaptive time step is chosen following the Courant-Friederichs-Lewy (CFL) criterion. The spatial numerical scheme is of fifth-order accuracy for a smooth gradient of velocity field if the fourth-order scheme is chosen. However, the model accuracy would decrease due to utilizing limiters in the TVD-type scheme. The numerical diffusion is mainly from the reduced numerical accuracy when a sharp gradient of flow field occurs.

A moving shoreline is modeled by a wetting-drying scheme based on the local surface elevation versus water depth. The normal flux at the wet-dry interface is set to zero. A mirror boundary condition is applied to the high-order MUSCL-TVD scheme and discretization of dispersive terms at a moving boundary. The wave speed of the Riemann solver at the wet-dry interface is modified according to Zhou et al. (2001).

5 Benchmark Problem Comparisons

Altogether, five benchmark tests were developed for use in the workshop, of which the first two were required of participants. Model-data and inter-model comparisons for these first two tests have been documented in Lynett et al. (2017). The tests include

1. Shallow, open channel flow over an isolated bump (Lloyd and Stansby, 1997).
2. Wave and current motion in Hilo Harbor, Hawaii following the 2011 Tohoku-oki tsunami (Cheung et al., 2013)

3. Tsunami and tidal current interaction in Tauranga Harbor, New Zealand, a multiple inlet coastal lagoon (Borrero et al., 2012)
4. Inundation of a laboratory model of Seaside, Oregon by a solitary wave (Park et al., 2013)
5. Run-up of a solitary wave on a wedge-shaped coastal promontory (Swigler,).

FUNWAVE-TVD results for each of these five cases are described in the following sections.

5.1 Steady flow over a submerged obstacle

Lloyd and Stansby (1997) conducted a number of experiments on steady open channel flow past a conical shoal in an otherwise uniform rectangular channel. The channel geometry is shown in Figure 1. The experiments were conducted for a range of water depths and included cases with both emergent and submerged shoals. The benchmark case here is based on Case SB4.02 of Lloyd and Stansby (1997). In this test, with a submerged shoal, a wake consisting of a mean flow deficit together with a nearly regular vortex street was generated. Measurements consisted of surface velocities derived from optical imagery of floating tracers, with time series provided at two locations shown in Figure 1, one downstream of the shoal on the channel centerline, and a second displaced X cm off the centerline at the same downstream location.

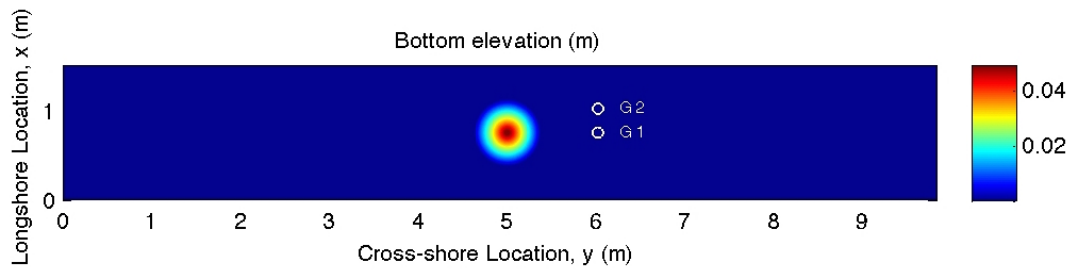
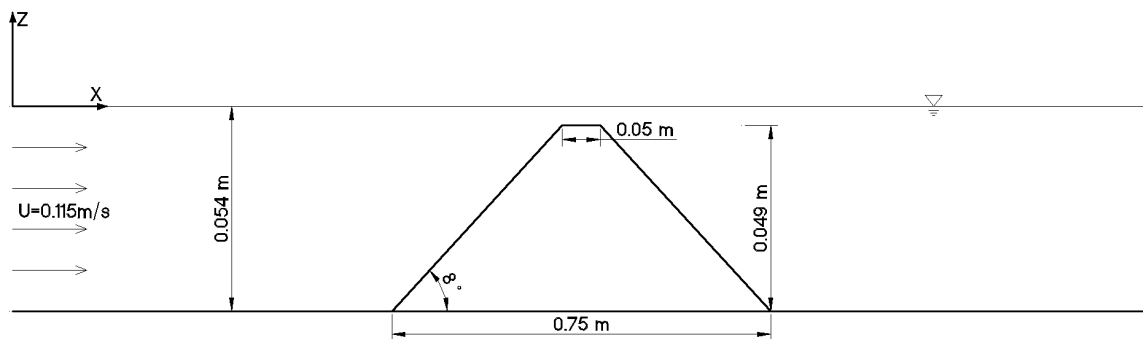


Figure 1: Geometry of experiments of Lloyd and Stansby (1997a,b).

5.1.1 Model configuration

FUNWAVE-TVD was set up in a computational domain with a width of 1.52m and length of 9.78m. A steady discharge velocity of 0.115 m/s was specified at the upstream boundary. At the downstream boundary, a radiation boundary condition was applied. The radiation boundary condition for the Riemann solver was implemented using the zero-gradient condition for surface elevation and velocity components according to Toro (2009).

5.1.2 Numerical results

Several tests were carried out with different bottom friction coefficients ($C_d = 0.0, 0.003, 0.006, 0.012$), different grid resolutions (0.005m, 0.01m, 0.03m) and CLF conditions (CLF=0.25, 0.5). The model convergence tests showed that model results were unaffected by the grid size reduction from 0.01m to 0.005m and the CLF reduction from 0.5 to 0.25. The optimal bottom friction coefficient was found to be $C_d = 0.012$ based on model/data comparisons of velocity components at measurement locations. The experimental time series are displayed in Figurefig2 together with numerical predictions of the reference elevation velocity \mathbf{u}_α .

The model is seen to underpredict the value of mean flow in the streamwise at the gauge location 1 directly downstream of the shoal. This underprediction is much greater than the error expected in comparing measurements at elevation $z = 0$ to simulated values at elevation $z = z_\alpha = -0.53h$, as further evidenced by the lack of disagreement at the Gauge 2 and in the transverse component of velocity v at gauge 1. This error is repeated in all of the depth-integrated model formulations shown in the workshop, and indicates the presence of a structural deviation in the flow field away from the form assumed in the

Boussinesq model development.

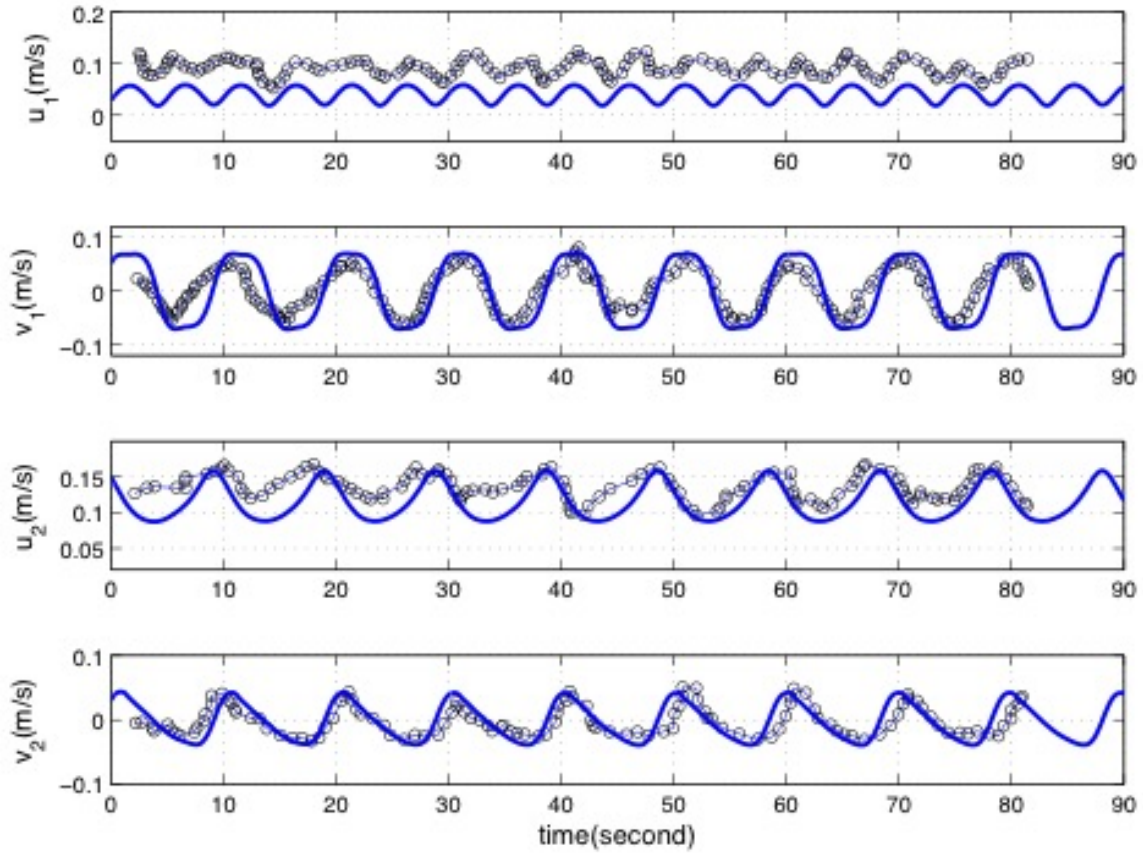


Figure 2: Experimental data (dots) and numerical simulation (solid line, not shown) for a) u velocity component at time series location 1, b) v velocity component at time series location 1, c) u velocity component at time series location 2, and d) v velocity component at time series location 2.

Point Name	Abbreviation	E Lon.	N Lat.
Control Point	CP	204.93	19.758
Tide Gauge	TG	204.94	19.73
ACDP1	ACDP1	204.92	19.74
ACDP2	ACDP2	204.93	19.74
Dart Buoy #51407	DB	203.49	19.62
Near Hilo Harbor station	NHHS	204.95	19.75

Table 1: Definition and location of numerical wave gages used in FUNWAVE-TVD simulations.

5.2 Tsunami currents in Hilo Harbor

In this benchmark test, currents and surface displacements resulting from the Tohoku-oki 2011 event were simulated in Hilo Harbor, Hawaii. Data consists of surface displacements at the harbor tide gage along with current measurements collected by two profiling ADCP's which were installed for separate scientific studies. The harbor layout and instrument locations are indicated in Figure 3. Previous model simulations have been carried out by Cheung et al. (2013) and were used in the workshop benchmark specification to provide input conditions at the control point CP shown in Figure 3. This data was intended for use as the input data for smaller scale simulations centered on the harbor. Table 1 provides coordinates for instruments and control points used as part of the simulations.

This benchmark was simulated using two separate procedures. The first procedure, referred to as the *local simulation*, followed the original suggested procedure for the benchmark. Simulations were driven by a time series of free surface elevation provided at the control point CP (Figure 3).

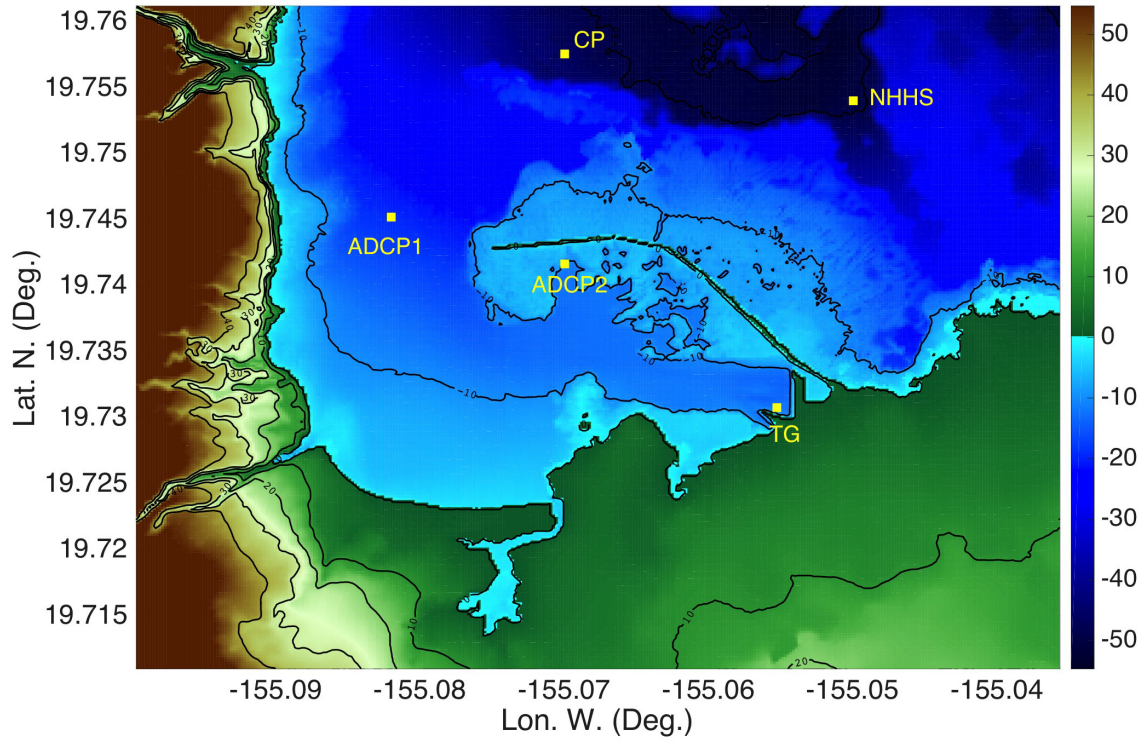


Figure 3: Footprint of Hilo Harbor computational grids G4 (20 m), G5 (10 m), G6 (5 m) (Table 2) with location of control point (CP), tide gage (TG), ADCPs (ADCP1, ADCP2), and Near Hilo Harbor Station (NHHS) (Table 1).

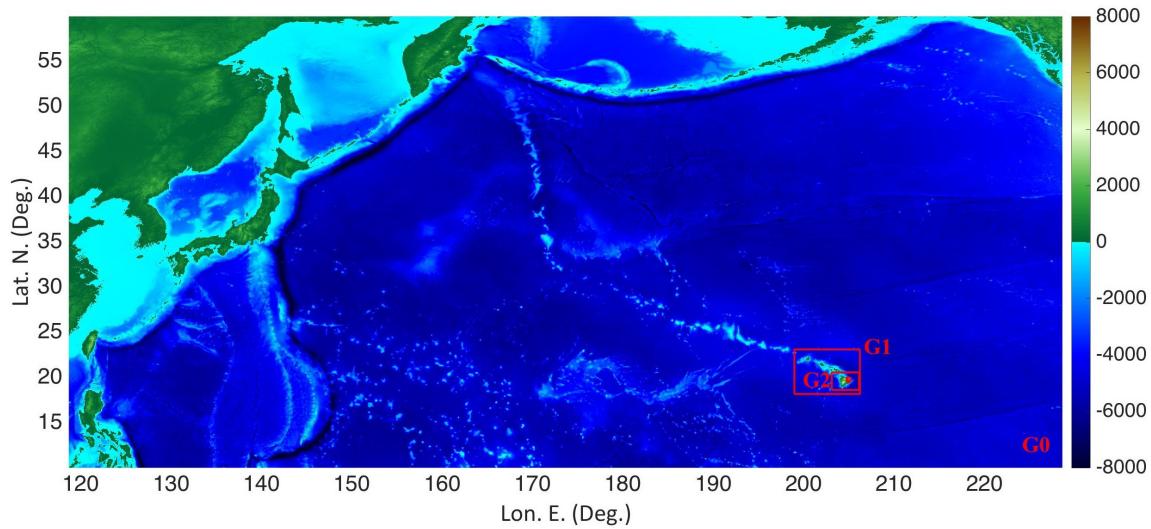


Figure 4: Footprints of nested computational grids G0 to G3 (Table 2). Color scale is bathymetry (< 0) and topography (> 0) of grid G0 in meter.

In the second procedure, referred to as the *global simulation*, the entire Tohoku-oki event was simulated, from source region to eventual arrival in Hilo Harbor. The Tohoku tsunami source was obtained from earlier work (Grilli et al., 2013; Kirby et al., 2013; Tappin et al., 2014).

5.2.1 Numerical model configuration

A series of nested grids G0 to G6 were constructed based on publicly available bathymetry data. Grid dimensions and resolutions are listed along with data sources in Table 2. Figures 4 - 6 show the nesting of the set of grids, extending from the source region to Hilo Harbor itself.

Grid Name	Resolution	Footprint Coordinates	Cartesian/Spherical	Bathymetry source
G0	2 arc-min	(118.68 E, 131.36 W); (10.01 S, 60 N)	Spherical	ETOPO1 (1' arc)
G1	30 arc-sec	(198.5 E, 153 W); (17.8 S, 23.1 N)	Spherical	GMRT- 114 m
G2	7.5 arc-sec	(154.04 E, 156.88 W); (18.63 S, 20.58 N)	Spherical	GMRT- 57 m
G3	55 m	(154.84 E, 155.25 W); (19.55 S, 19.99 N)	Cartesian	Hilo Benchmark
G4	20 m	(155.1 E, 155.036 W); (19.71 S, 19.76 N)	Cartesian	Hilo Benchmark
G5	10 m	(155.1 E, 155.036 W); (19.71 S, 19.76 N)	Cartesian	Hilo Benchmark
G6	5 m	(155.1 E, 155.036 W); (19.71 S, 19.76 N)	Cartesian	Hilo Benchmark

Table 2: Parameters of numerical grids used in FUNWAVE-TVD simulations (GMRT data was obtained from <http://www.marine-geo.org/tools/GMRTMapTool>)

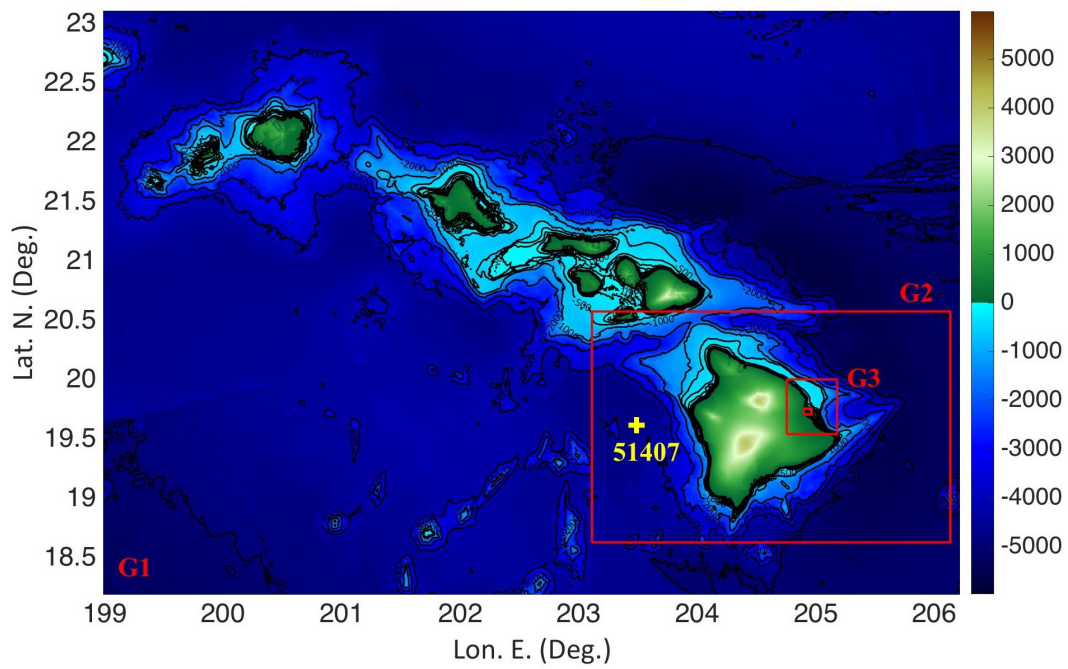


Figure 5: Footprints of nested computational grids G1 to G4 (Table 2). Color scale is bathymetry (< 0) and topography (> 0) of grid G1 in meter. Location of dart buoy #51407 is marked.

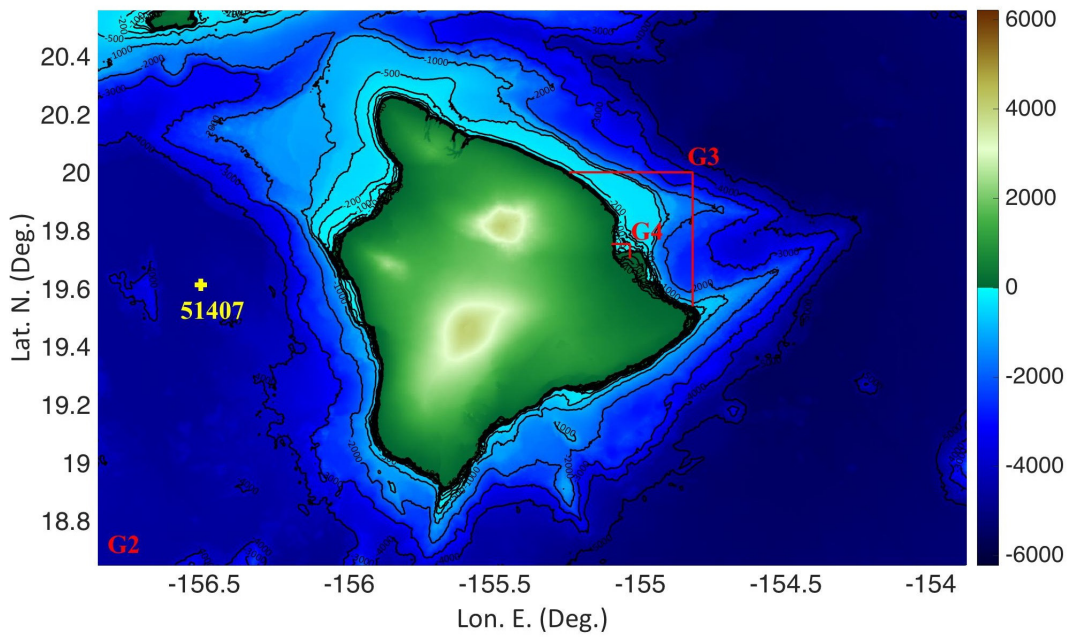


Figure 6: Footprints of nested computational grids G2 to G4 (Table 2). Color scale is bathymetry (< 0) and topography (> 0) of grid G2 in meter. Location of dart buoy #51407 is marked.

5.2.2 Local simulations

Local simulations of the event were carried out on Cartesian grids G4, G5 and G6 with 20, 10 and 5m horizontal resolution, respectively. The bathymetry provided in the benchmark definition for Hilo Harbor was mapped to the Cartesian coordinate system using a transverse Mercator transformation (Figure 6).

Control point (CP; Fig. 6, Table 1) lies on the northern boundary of the computational grid, along which the free surface elevation was set to be the same as that of the control point, except for a correction to this elevation introduced to account for shallow water breaking. The horizontal current magnitude was specified along the offshore boundary based on linear long wave theory, for the corresponding elevation, initially in a boundary normal direction. A few iterative simulations were performed to estimate both the reflection coefficient and wave angle of incidence (which affects velocity components), by trial and error.

Figure 7 shows comparisons of modeled surface elevation time series to the provided benchmark data at CP for computations in grids G4 to G6 at CP. The agreement between results of simulations in grids G4-G6 is very good, indicating that surface elevations are not very sensitive to increasing grid resolution in the region outside the harbor. The overall agreement of these results with the benchmark data at CP is good, with a root-mean-square (rms) error between the benchmark data and the simulations of about 0.08 m for all three grids, relative to a maximum elevation of incident waves of over 1 m. However, there are significant local discrepancies, particularly for the first few tsunami waves.

Figure 40 compares the time series of surface elevation computed in grids G4 to G6 using the iterated inflow conditions at CP, at the tidal gage (TG; Figure 6, Table 1), both

with each other and with the provided benchmark data. As before, the agreement of free surface elevations computed in grids G4-G6 is very good. However the agreement of computations with field data is only good for the first 2 waves in the tsunami train, between 1.5 to 2.3 h, with increasing discrepancies in both elevation and phase later in time. As a result, the rms error between simulations and field data is about 0.5 m in each grid, with the maximum elevation of the wave being about 2 m.

Figures 9 to 12 compare time series of velocity component or velocity magnitude computed in grids G4 to G6 using the iterated inflow conditions at CP, at the two ADCPs (ADCP1 and ADCP2; Figure 3, Table 1), both with each other and with field data. First, we see that the effects of grid resolution has a larger impact on the computed velocities than for surface elevations. This is also confirmed in Figure 14, which shows the envelopes of maximum horizontal current magnitude computed for the entire simulations in each grid. Based on these results, at ADCP1, the rms difference of velocity magnitude between results of the G4 (20 m) and G5 (10 m) grids is about 0.01 m/s, whereas it is about 0.06 m/s between results of the G5 (10 m) and G6 (5 m) grids. At ADCP2, the rms differences between each pair of grids is about 0.06 m/s. Note, at both ADCP locations, the maximum velocity is on the order of 1 m/s.

Looking more closely at the envelopes in Figure 14, however, it is clear that while differences in computed maximum velocities in each grid are small over most of the computational grids, they become larger near and around the tip of the Hilo breakwater, from which eddies are spawned that are strongly grid dependent. Due to the proximity of these eddies to the two ADCPs (Figure 3), the differences in size and propagation patterns of the eddies cause large differences in the predicted velocities at the location of the 2 ADCPs.

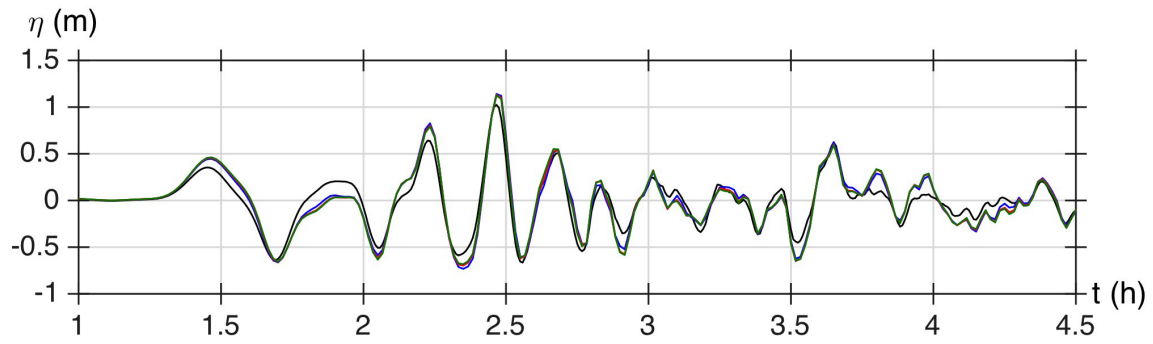


Figure 7: *Local simulations.* Comparison of time series of surface elevation computed in grids G4 (green), G5 (red) and G6 (blue) at the Control Point Station (CP; Fig. 6, Table 1), with each other and with the benchmark data (black).

As a result of the sensitivity of the computed eddies to grid resolution, in the time series of velocity component or velocity magnitude in Figures 9 to 12, we observe large discrepancies, particularly between results of simulations in grids G4-G5 and grid G6, and between these and the measured field data.

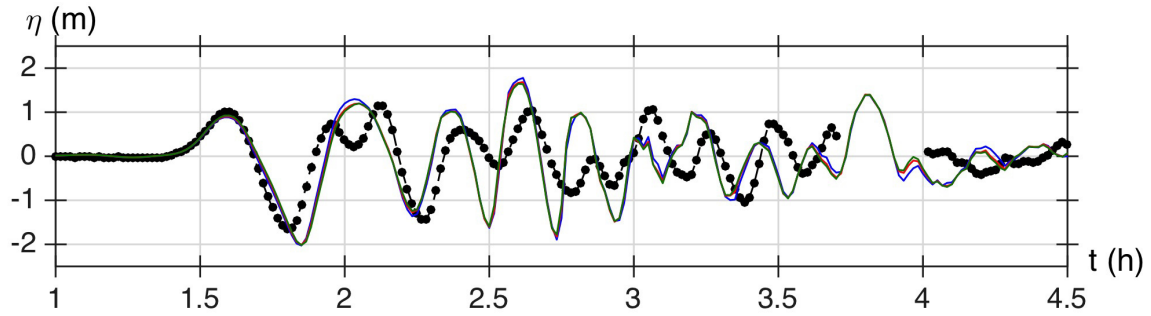


Figure 8: *Local simulations*. Comparison of time series of surface elevation computed in grids G4 (green), G5 (red) and G6 (blue) at the Tide Gage Station (TG; Fig. 6, Table 1), with each other and with field data (black with (•) symbols).

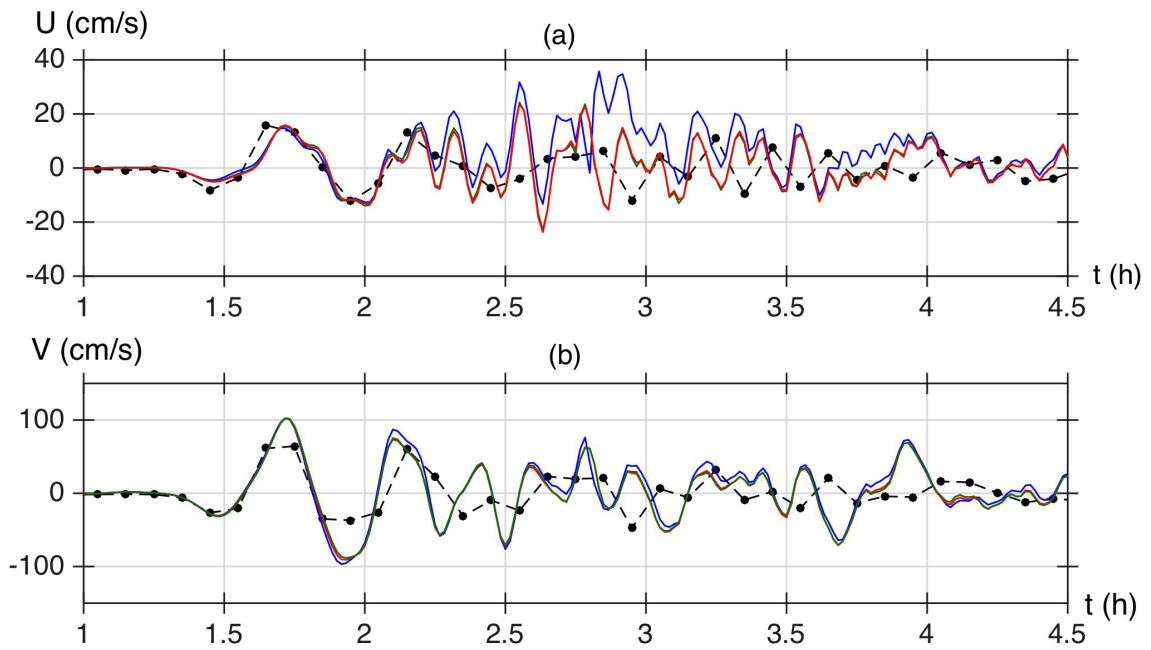


Figure 9: *Local simulations*. Comparison of time series of horizontal current (U , V) computed in grids G4 (green), G5 (red) and G6 (blue) at the ADCP1 Station (Fig. 6, Table 1), with each other and with field data (black with (•) symbols).

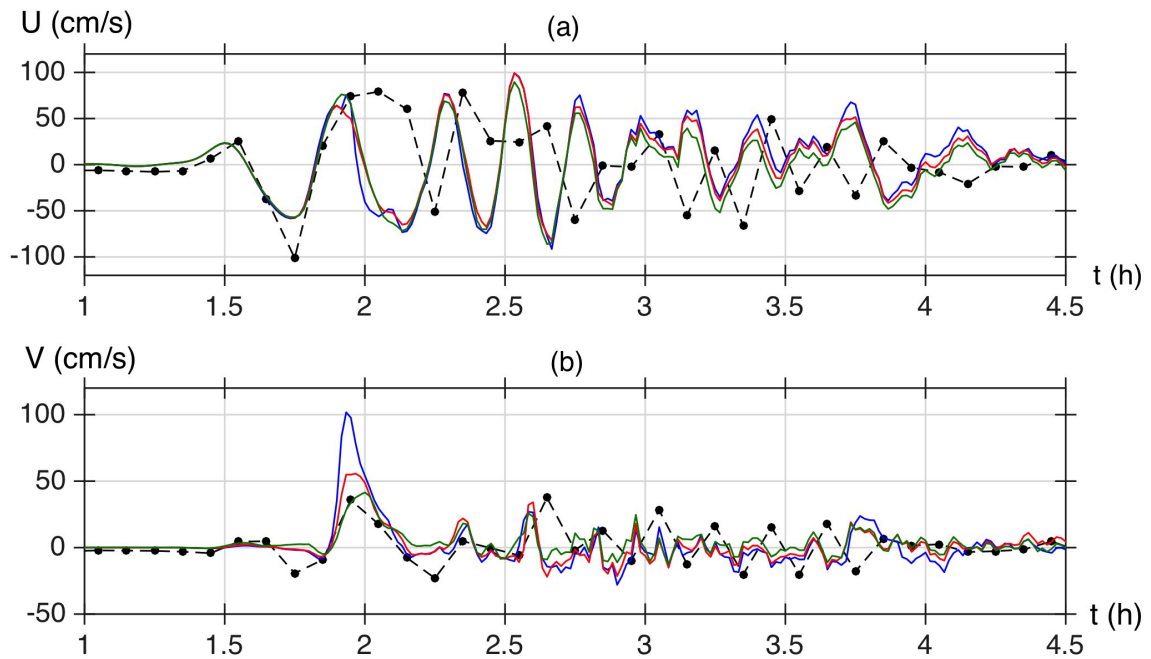


Figure 10: *Local simulations*. Comparison of time series of horizontal current (U, V) computed in grids G4 (green), G5 (red) and G6 (blue) at the ADCP2 Station (Fig. 6, Table 1), with each other and with field data (black with (•) symbols).

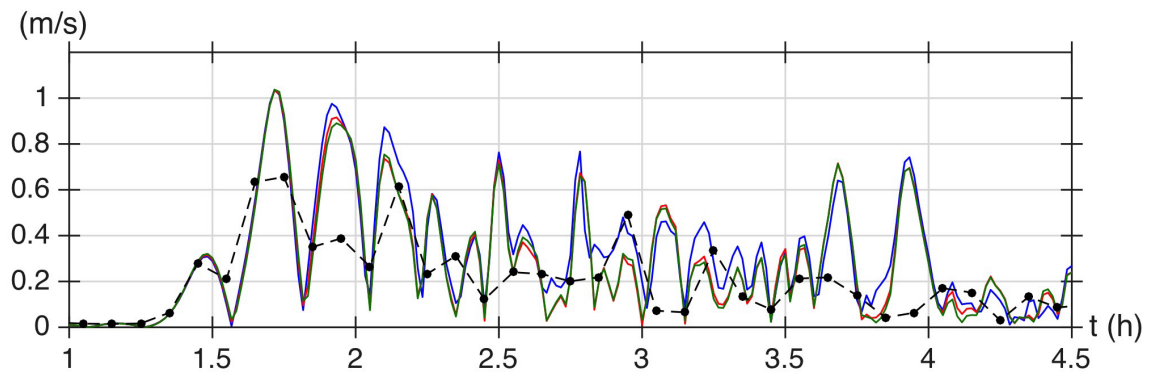


Figure 11: *Local simulations*. Comparison of time series of horizontal current magnitude computed in grids G4 (green), G5 (red) and G6 (blue) at the ADCP1 Station (Fig. 6, Table 1), with each other and with field data (black with (•) symbols).

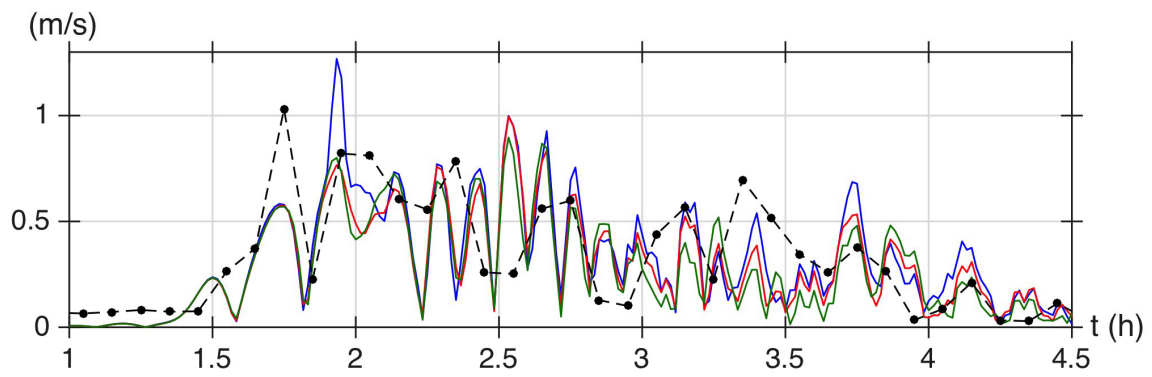


Figure 12: *Local simulations*. Comparison of time series of horizontal current magnitude computed in grids G4 (green), G5 (red) and G6 (blue) at the ADCP2 Station (Fig. 6, Table 1), with each other and with field data (black with (●) symbols).

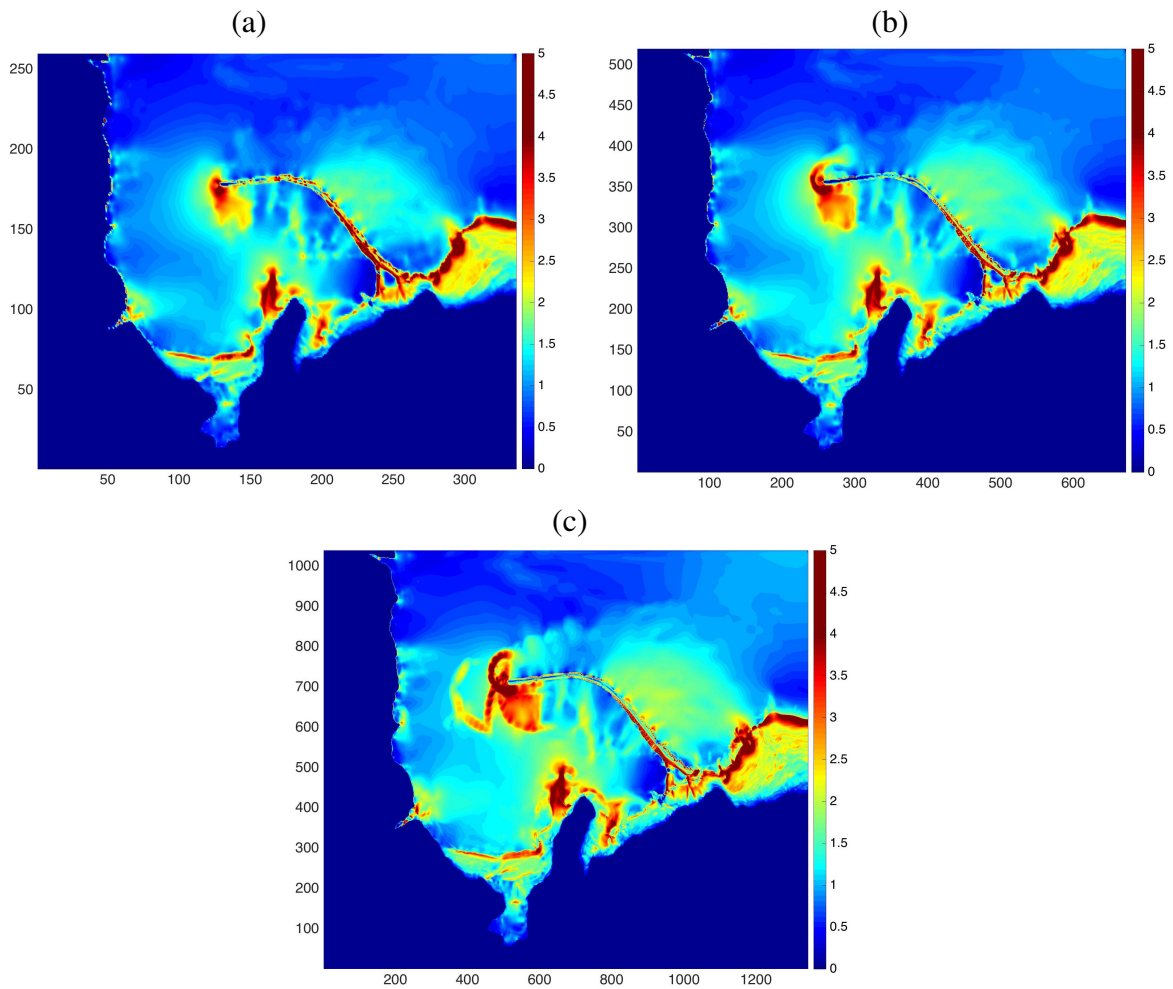


Figure 13: *Local simulations*. Envelopes of maximum horizontal current magnitude computed for the entire simulations in grids : (a) G4 (20 m), (b) G5 (10 m) and (c) G6 (5 m). Note that axes are numbered with the Cartesian grid cell indices.

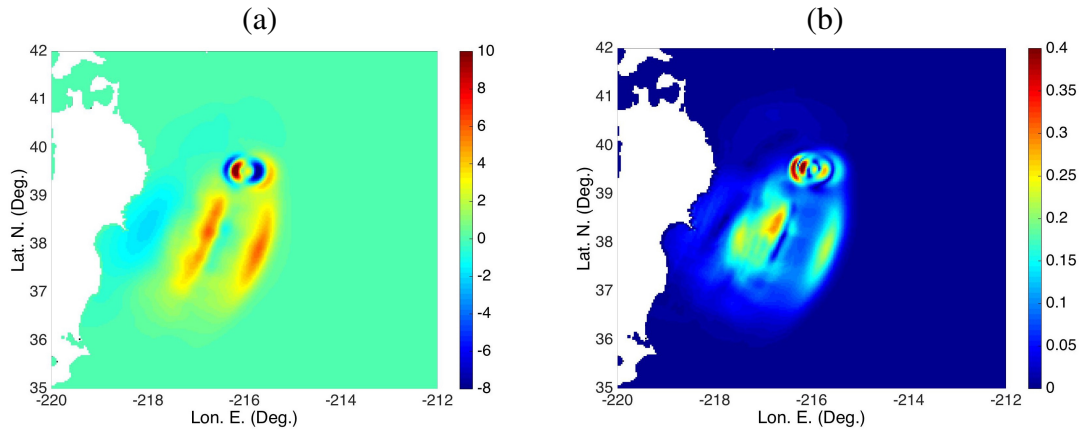


Figure 14: Source of the Mw 9.1 Tohoku 2011 event computed with NHWAVE at 300 s after the earthquake (Grilli et al. 2013; Tappin et al., 2014): (a) sea surface elevation (m); and (b) horizontal velocity magnitude (m/s). Note the long-crested seismic waves generated to the south by the earthquake and the shorter-dispersive cylindrical waves generated to the north by the secondary SMF mechanism.

5.2.3 Global simulations

In the global simulations, the boundary condition along the offshore boundary of the Hilo grids G4-G6 (Fig. 3) was specified based on modeling the Tohoku 2011 tsunami propagation from its source to Hilo Harbor. The Tohoku tsunami source was obtained from earlier work (Grilli et al., 2013; Kirby et al., 2013; Tappin et al., 2014), in the form of the surface elevation and horizontal current computed at 300 s based on a dual coseismic-submarine mass failure source (Fig. 14).

Simulations were performed with FUNWAVE-TVD, by one-way coupling, in a series of nested spherical then Cartesian grids of increasing resolution (G0 to G4 in Table 1 and Figs. 4 to 6). In these grids, increasingly resolved bathymetry and topography data was

used as described in Table 2. In the coarser grid G0, the surface elevation and horizontal velocity of the Tohoku 2011 tsunami source were specified as initial condition. To eliminate reflection, 100 km thick sponge layers were specified along the open ocean boundary of the grid. Simulations were then pursued by one-way coupling in grids G1 to G3 and time series of surface elevation and current were computed along the offshore boundaries of grid G4. These were used to perform the required simulations in grids G4-6.

To verify that simulations in nested grids were accurately performed, we first compared time series of surface elevations computed in grids G0, G1 and G2 at Dart Buoy #51407 (Fig. 5; Table 1), both with each other and with field data. This is shown in Fig. 15, where we observe a good agreement of numerical results with each other and a reasonable agreement of those with field data (once a 2 min time shift is applied).

Simulations in the finer Cartesian grids G4 to G6 (Table 2; Fig. 6), with resolution 20, 10 and 5 m, were then run over the same area of Hilo harbor and with the same offshore boundary, over which both surface elevation and horizontal velocity computed in grid G3, were specified as time series at every grid point. Simulations results were then compared as before with the benchmark reference data.

To verify that these finer grid simulations were consistent with each other, time series of surface elevations predicted at the Near Hilo Harbor Station (NHHS) were compared. This is done in Figure 16, where we observe a good agreement between all these results, even in the tail of the time series, which is strongly affected by reflection from the coast.

Figures 17 and 18 show the comparison of time series of surface elevations computed at the Control Point station (CP; Figure 3; Table 1) and at the Tide Gage station (TG; Figure 3; Table 1), in grids G4 to G6, with each other and with independent simulations

or field data, respectively. All simulation results agree well with each other at CP and TG, indicating that increasing resolution in grids G4 to G6 does not significantly affect the simulation of surface elevations. In Fig. 17, the agreement of the present results with the independent simulations at the CP is initially quite good, but as time increases, discrepancies in both surface elevation and phase increase. In Figure 18, at the TG, simulations agree reasonably well with field data, particularly for the first 3 wave crests; beyond these, there appears to be an increasing phase shift between simulations and observations.

Figures 19 and 20 show the comparison of time series of horizontal current (U , V) computed at the ADCP1 and ADCP2 stations (Fig. 3; Table 1) in grids G4 to G6, both with each other and with field data. Here differences between each simulation made at a different resolution are larger, which as for the regular simulations is related to eddies of different size and dynamics being generated in the simulations near the tip of the Hilo breakwater, in the area of the two ADCPs, which are function of discretization. As a results, in Figs. 19 and 20, the agreement of the simulated velocity components with field data is again much less good than for surface elevations, although the overall trend is captured for the first few waves.

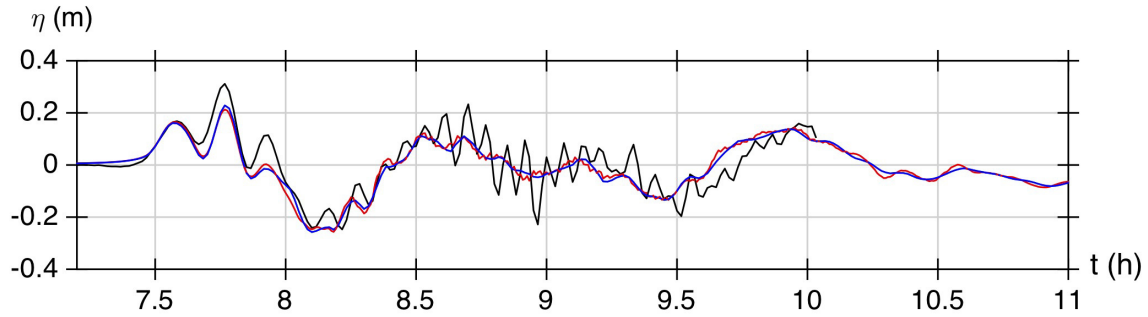


Figure 15: *Global simulations*. Comparison of time series of surface elevation computed in grids G0 (blue), G1 (green) and G2 (red) at Dart buoy #51407 (Fig. 6; Table 1), with each other and with field data (black). Note, results in grid G1 and G2 are indistinguishable. Numerical data is shifted 2 min backwards.

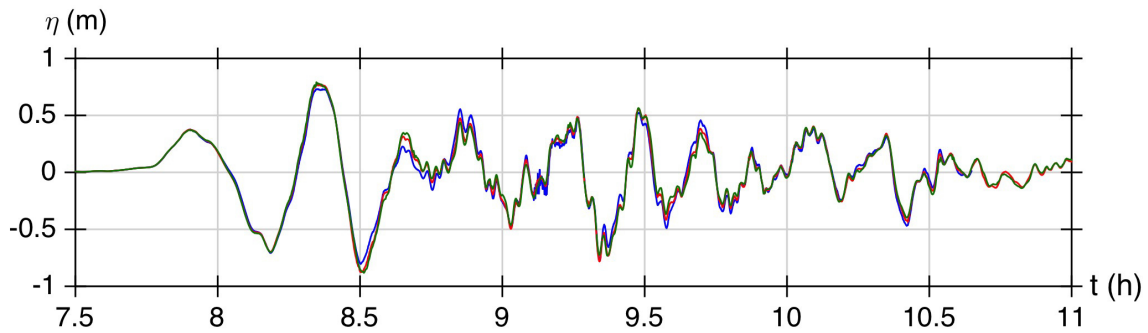


Figure 16: *Global simulations*. Comparison of time series of surface elevation computed in grids G4 (green), G5 (red) and G6 (blue) at the Near Hilo Harbor Station (NHHS; Fig. 3, Table 1), with each other.

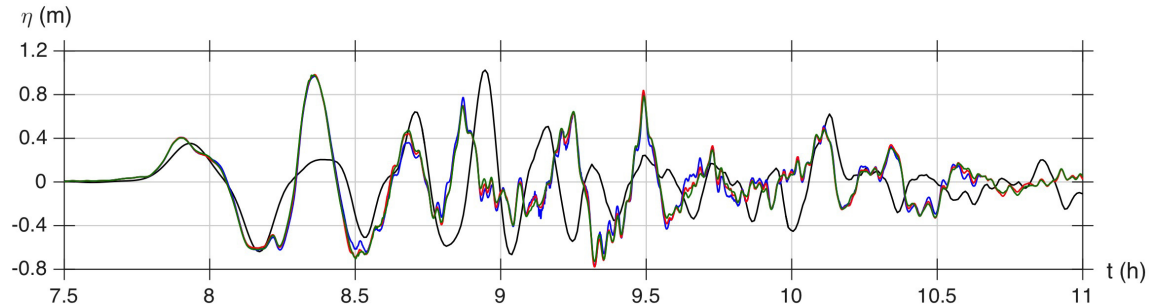


Figure 17: *Global simulations*. Comparison of time series of surface elevation computed in grids G4 (green), G5 (red) and G6 (blue) at the Control Point Station (CP; Fig. 3, Table 1), with each other and with field data (black). (simulation time was shifted by 5.8 min to improve phase match)

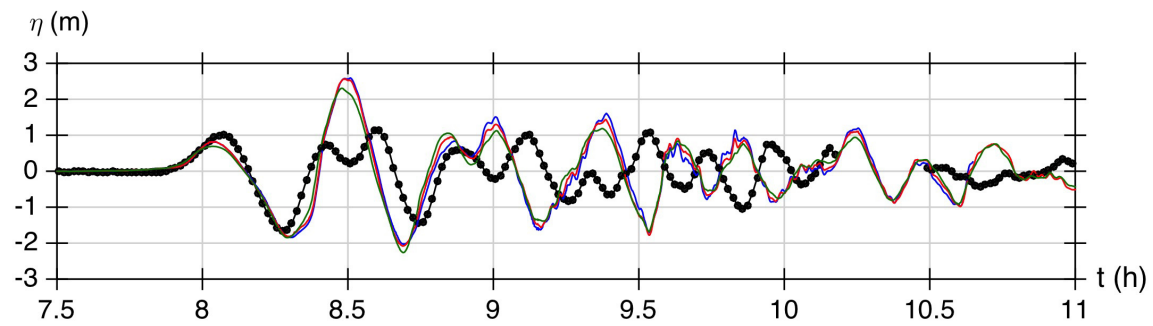


Figure 18: *Global simulations*. Comparison of time series of surface elevation computed in grids G4 (green), G5 (red) and G6 (blue) at the Tide Gage Station (TG; Fig. ??, Table 1), with each other and with field data (black with ● symbols). (simulation time was shifted by 5.8 min to improve phase match)

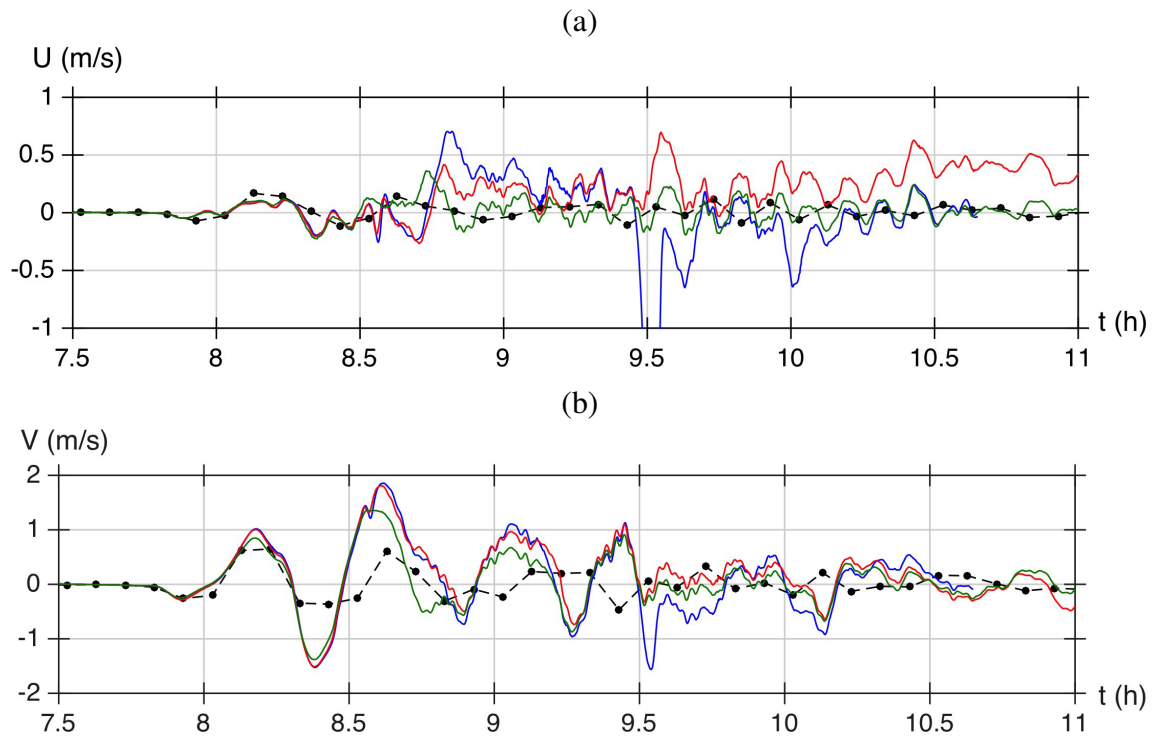


Figure 19: *Global simulations*. Comparison of time series of horizontal current (U, V) computed in grids G4 (green), G5 (red) and G6 (blue) at the ADCP1 Station (Fig. 3, Table 1), with each other and with field data (black with (●) symbols). (simulation time was shifted by 5.8 min to improve phase match)

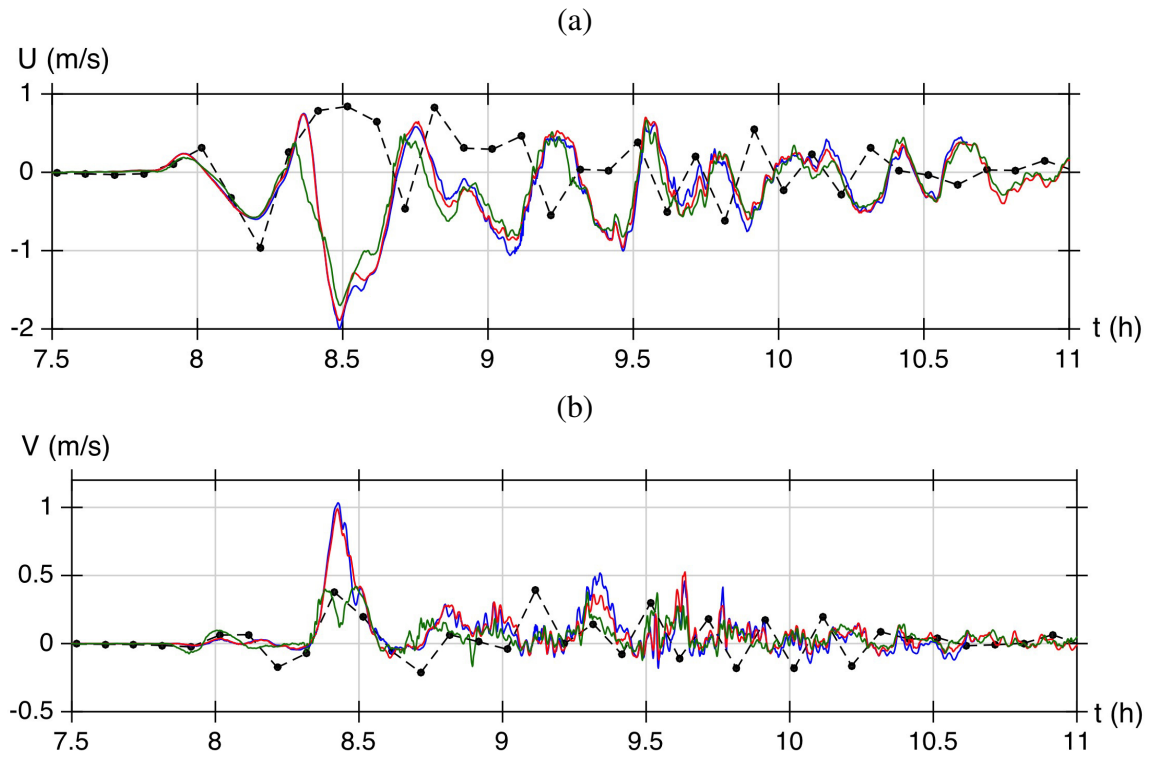


Figure 20: *Global simulations*. Comparison of time series of horizontal current (U, V) computed in grids G4 (green), G5 (red) and G6 (blue) at the ADCP2 Station (Fig. 3, Table 1), with each other and with field data (black with (•) symbols). (simulation time was shifted by 5.8 min to improve phase match)

5.3 Tsunami currents in Tauranga Harbor

The purpose of the Tauranga Harbor benchmark is to investigate the interaction between tide and tsunami. A general approach to this problem is to model tide and tsunami separately, then to linearly combine the signals along a boundary where depth is sufficient to allow for such a superposition. Benchmark data is provided at five locations, one for driving the simulations (A Beacon), and the remaining four for comparison with model results (Figure 21). Initially, a north-oriented grid was used to simulate tide. This approach was abandoned in favor of a grid aligned with the shore.

5.3.1 Introduction

Tauranga Harbor is separated from New Zealand's Bay of Plenty by a barrier island; two inlets connect the harbor to the bay (Figure 21). The city of Taruanga, several tide gage stations, and a buoy equipped with an ADCP are located near the easternmost inlet (see symbols in Fig. ??). The arrival of the Tohoku 2011 tsunami was measured by these various pieces of equipment, in terms of surface elevation at the tide gages and current magnitude at the ADCP. The purpose of this benchmark is to validate FUNWAVE-TVD simulations of this field case study, against those measurements, and in particular investigate the accuracy of model predictions as a function of grid resolution, while focusing on the velocity measurements, which are the main object of the benchmark.

Additionally, since this is an environment with strong tidal forcing, we will investigate effects of interactions between tide and tsunami by doing simulations for the tsunami alone, compared to de-tided measurements, and simulations of the tsunami together with the tidal forcing, compared to the actual measurements. For the latter, we will first run

and calibrate simulations for the tide alone. Then, assuming that both the incoming tide and tsunami, at a deep water offshore boundary, are linear long waves, we will linearly superimpose both their elevation and current to define the combined offshore boundary condition.

5.3.2 Definition of FUNWAVE-TVD model grids

A 40 meter resolution Cartesian grid (948 by 437 cells; SW corner coordinates: 37.5248° S, 175.8445° E) was first defined in FUNWAVE-TVD, more or less aligned with the barrier island to cover the benchmark area, with its outer offshore boundary intersecting the A-Bacon location where the incoming tsunami and tide were measured (Figure 21). The model was supposed to be forced by a boundary conditions representing a specified surface elevation along this boundary. A Beacon is in 25 meters of water, which is deep enough to combine tide and tsunami signals in a linear superposition, as indicated above. A second, 10 meter resolution, nested grid (504 by 404 cells; SW corner coordinates: 37.6319° S 176.1442° E) was defined to assess effects of increased resolution on model results (Figure 21); this grid includes all data comparison points, except A Beacon, which serves to force simulations in the 40 meter grid. Each of the four sides of this 10 m grid had boundary conditions specified based on results from the 40-meter grid.

Nested grid simulations are performed by one-way coupling, in which time series of surface elevation and depth-averaged current are computed for a large number of stations/numerical wave gages, defined in a coarser grid, along the boundary of the finer grid used in the next level of nesting. Computations are fully performed in the coarser grid and then are restarted in the finer grid using the station time series as boundary con-

ditions. As these include both incident and reflected waves computed in the coarser grid, this method closely approximates open boundary conditions. It was found in earlier work that a nesting ratio with a factor 3-4 reduction in mesh size allows achieving good accuracy in tsunami simulations (a nesting factor of 4 is used here). In all simulations, bottom friction was specified based on Mannings formula using a constant Manning coefficient $n = 0.025$.

In initial simulations, the very steep bathymetry at the loading docks on the edge of the rightward dredged channel was found to lead to some instabilities in model results. Rather than using a bathymetry with a moving shoreline along the docks, a no-flux boundaries was specified using the obstacle option of FUNWAVE-TVD. This boundary condition was specified in both the 40 meter and 10 meter grids (Figure 21).

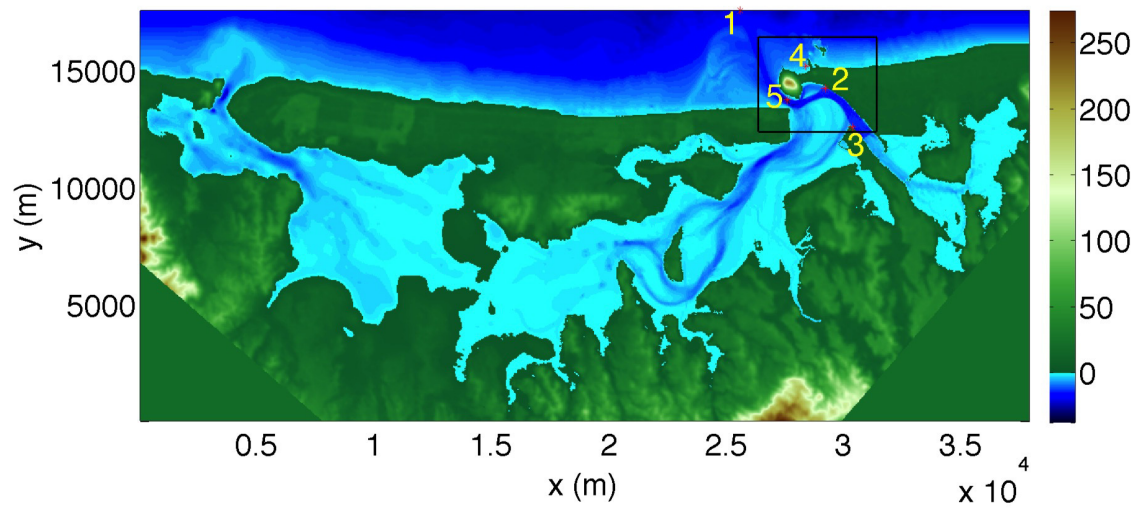


Figure 21: Shore-oriented (x) bathy/topo (color scale in m) of 40 m Cartesian FUNWAVE-TVD grid, with a 10 m nested Cartesian grid (black box). Locations of measuring equipment are shown as red dots. Tide stations are marked as follows: (1) A Beacon, (2) Tug Berth, (3) Sulfur Point and (4) Moturiki. An ADCP buoy is anchored in the middle of the inlet (slack mooring) at dot marked (5). A-Beacon provides the inflow boundary conditions along the upper offshore boundary.

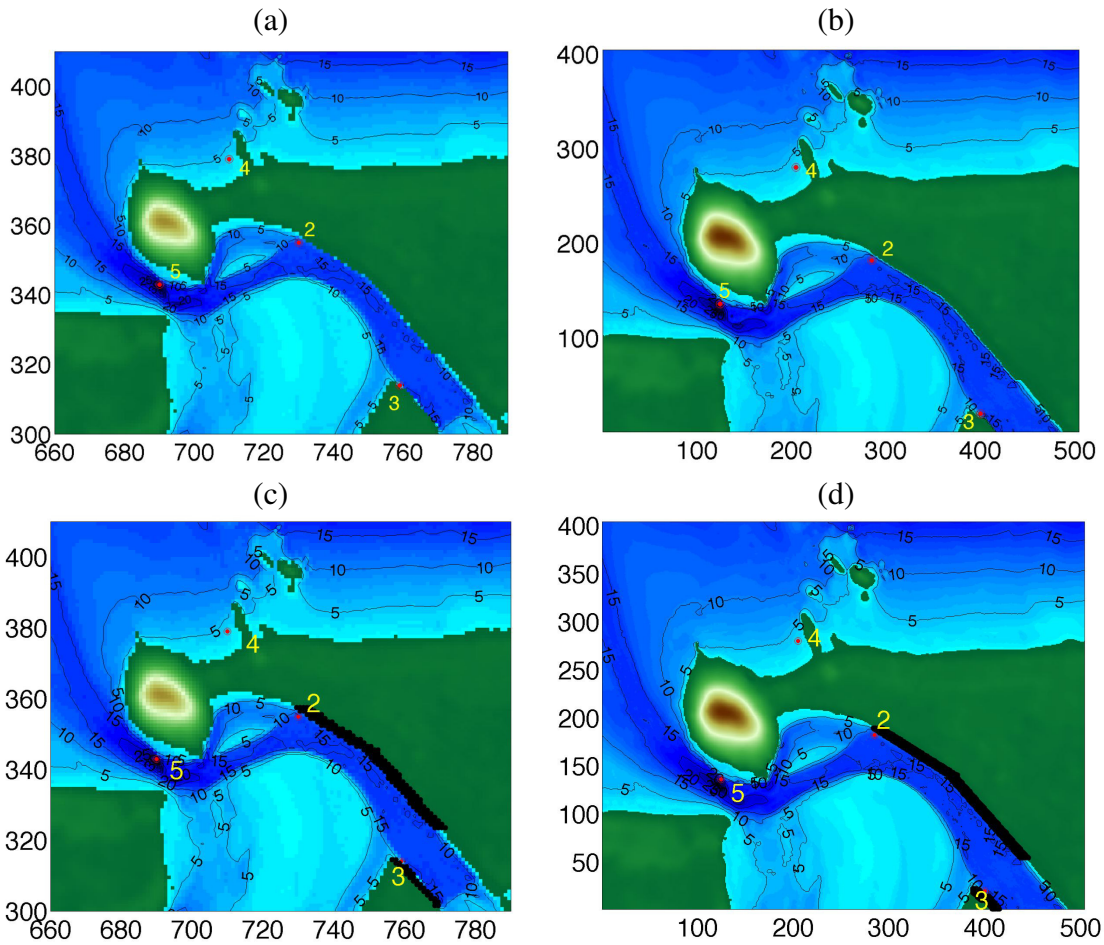


Figure 22: Zoom-in of (a,c) 40 meter; and (b,d) 10 m resolution Cartesian grids (axes are numbered by cell numbers), without and with an obstacle boundary. The obstacles (no-flux boundary condition shaded in black) were inserted in place of the steep bathymetry at the shore, near the stations marked (2) and (3). The location of data comparison points are indicated with red marks. From left to right, these points are: (5) ADCP Buoy, (4) Moturiki, (2) Tug Berth, and (3) Sulfur Point. A Beacon is located to the northeast.

5.3.3 Results: Tsunami simulations

Detided incoming tsunami surface elevation was provided at the *A beacon* for this benchmark as input data (Figure 23a). For modeling the tsunami alone, we specified this surface elevation along the entire offshore boundary of the 40 meter grid. Since no velocity was provided, we initially assumed that the current magnitude could be obtained based on a linear long wave approximation, $U = \eta\sqrt{g/h}$, with η the surface elevation, g the gravitational acceleration, and h the local depth; we also assumed that the current was directed towards shore, perpendicular to the offshore boundary (Figure 24).

A first model run showed differences between the specified and computed surface elevation and current on the offshore boundary at A Beacon, in part due to reflected waves from the barrier island, in the model. While keeping the measured free surface amplitude as a boundary condition, the specified current was iteratively corrected, using the average of the computed and specified velocities at each boundary grid point. This velocity averaging process was repeated in the 40 m grid simulations, until convergence was obtained (after 4 iterations; Figures 23a and 24). Simulations in the 40 m grid were then run for the 28 h for which tsunami data was available. At this point, nested simulations were performed in the 10 m grid based on the converged 40 m grid results.

Figure 25 shows surface elevations computed in the tsunami only simulations, in the 40 m and 10 m grids, at the (a) A Beacon (only in 40 m grid), (b) Tug Berth, (c) Sulfur Point, (d) Moturiki locations, compared to the detided measured surface elevations. We see a good agreement between these, and more particularly so for the 10 m grid results.

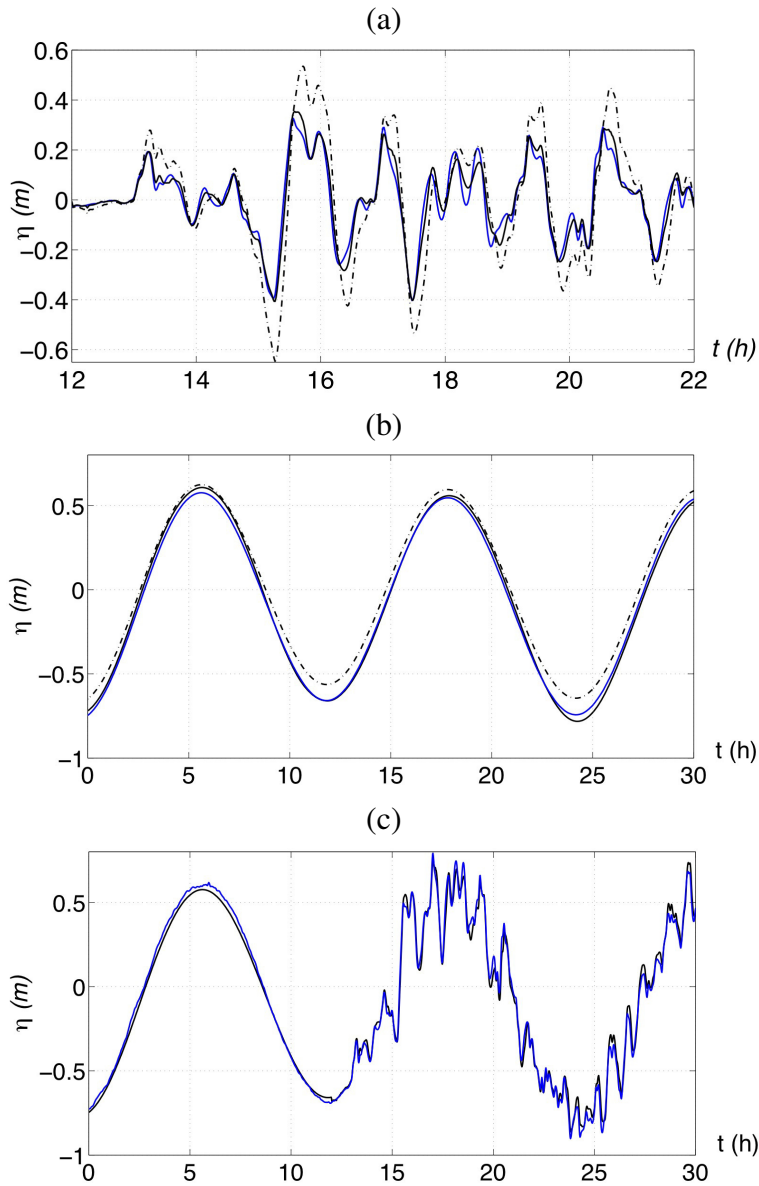


Figure 23: (a) Tsunami only simulations: initial discrepancy between specified surface elevation at A Beacon (black solid line), based on tsunami observations, and surface elevations computed with FUNWAVE-TVD (chained line); converged boundary condition (blue solid line line). (b) Tide only simulation: tide data at A Beacon (black solid line); OTPS model prediction (chained line); and the same corrected by 4% (blue solid line) used as a boundary condition. (c) Tsunami plus tide simulation: combined surface elevation specified as a boundary condition (black solid line) at A Beacon, compared to values computed in FUNWAVE-TVD (blue solid line).

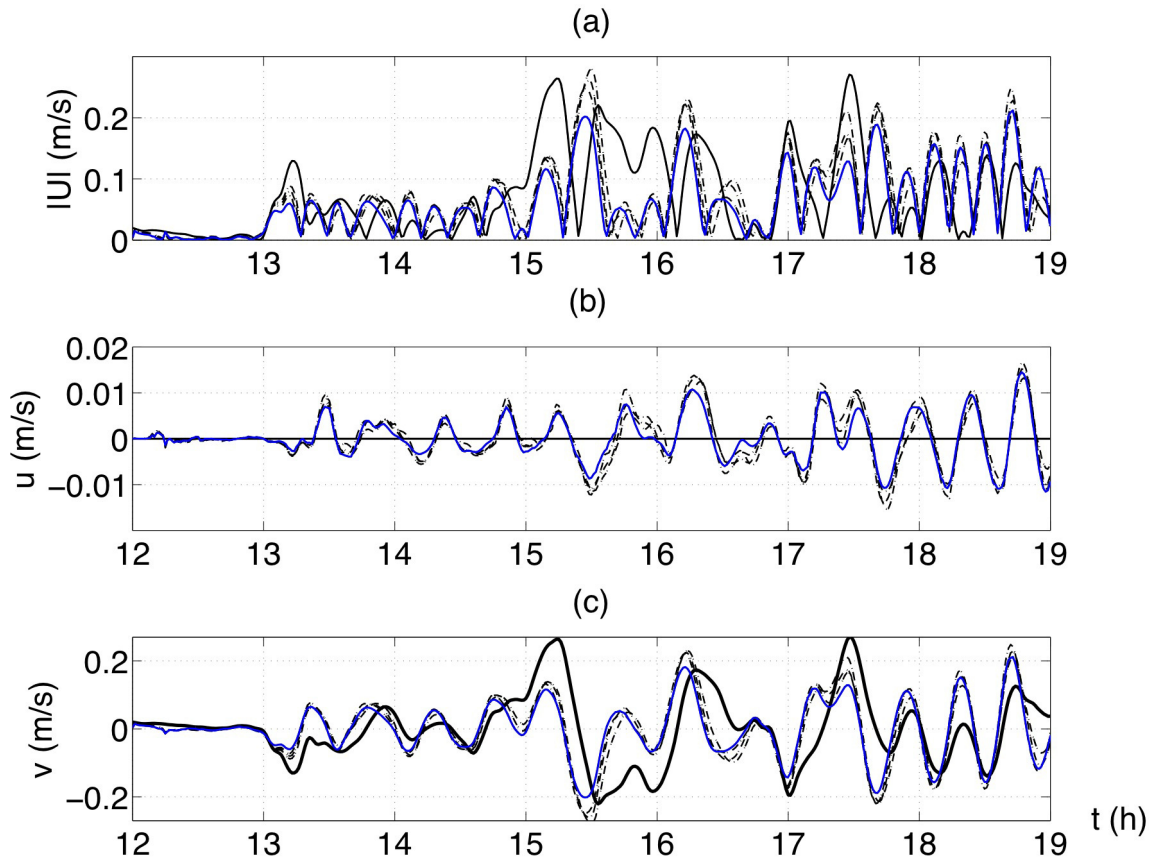


Figure 24: Tsunami only simulations: convergence of boundary condition for the input velocity module, (a) $|U|$ and components (b) u and (c) v , at A Beacon, in successive simulations in FUNWAVE-TVDs 40 m grid offshore boundary. Initial input velocity, based on a linear long wave approximation (black solid line), successive computations (dashed line), and the final input boundary condition (blue solid line).

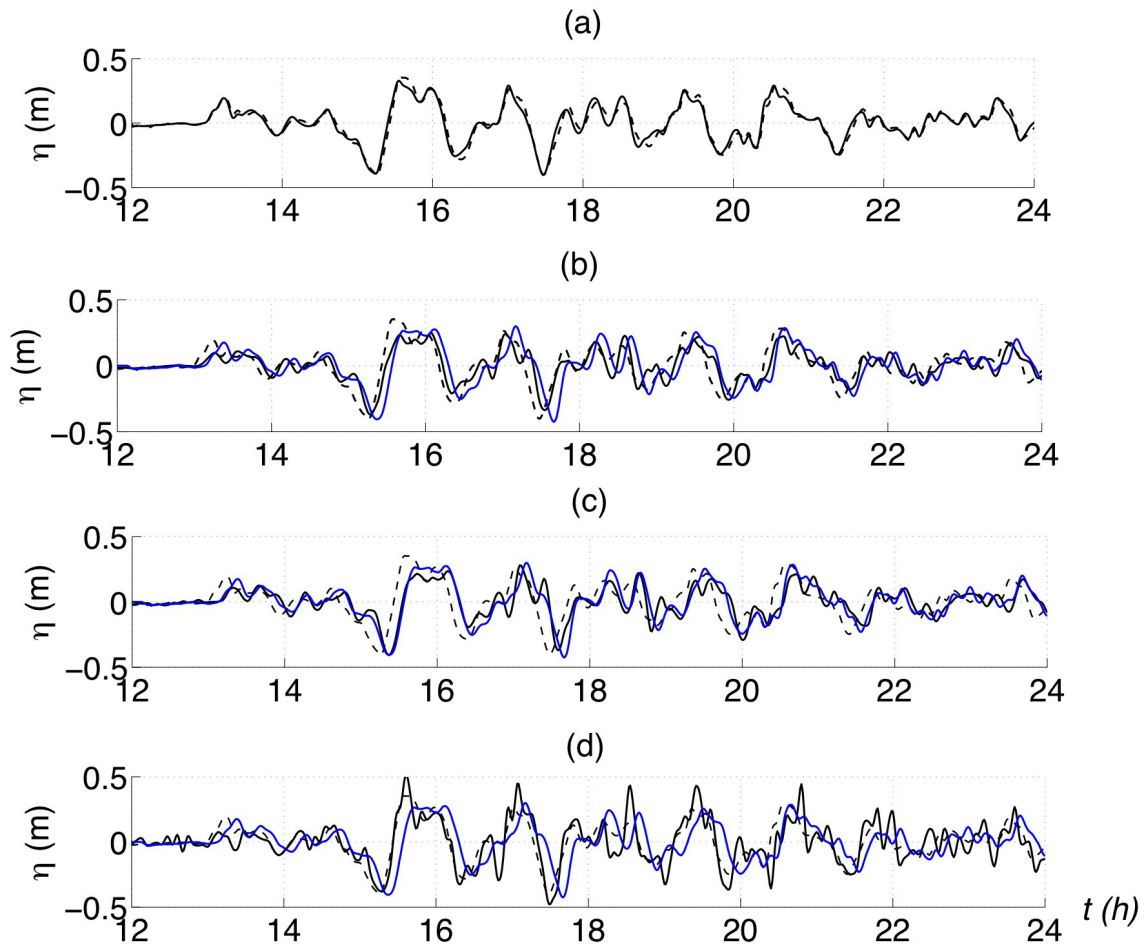


Figure 25: Tsunami only simulations. Measured tsunami surface elevations (solid line), detided and compared to FUNWAVE-TVDs 40 meter grid results (dashed line) and 10 meter grid results (blue solid line), at four locations: (a) A Beacon, (b) Tug Berth, (c) Sulfur Point, (d) Moturiki.

5.3.4 Results: Tide simulations

Because tide data was only provided at A Beacon for this benchmark, we used the Oregon Tide Prediction Software (OTPS) created by Erofeeva and Egbert (proper reference) to compute tide, surface elevation and current as a function of space and time. This model requires the Latitude and Longitude of data where the tide is to be computed; here, these are the grid points of the 40 m grid along the upper offshore boundary in Figure 21. The boundary stations in the 40 m grid were rotated into a north-oriented Cartesian grid, with units of meters, then projected onto the Earth ellipsoid. The center of projection was taken to be the A Beacon, at 37.60287° S, 176.17781° E. The OTPS model generated tidal surface elevations and currents for the resulting coordinates, shown in Figure 23b). The velocity data was rotated back into the shore-oriented reference frame, and together with surface elevation, both were scaled down by a factor 0.96, in order to better match the measured tide time series at A Beacon. This data was used to set boundary conditions in the tide-only FUNWAVE simulation, and later on, combined with tsunami data to perform the tide-tsunami interaction simulations (Figure 23c).

In FUNWAVE-TVD, both the tide surface elevation and current data used as boundary conditions along the 40 m grid offshore boundary were ramped up from zero over a 6 h period (using a tanh function), then allowed 12 h to stabilize. This 12 h stabilizing period was set between the time of the earthquake and the beginning of the tsunami signal in Tauranga. The remaining 28 h of simulation data overlapped the 28 h simulated in the tsunami only simulation. The obstacle and Manning friction were included in this simulation, similar to the tsunami only simulations.

Figure 26 shows surface elevations computed in the tide only simulations, in the 40 m

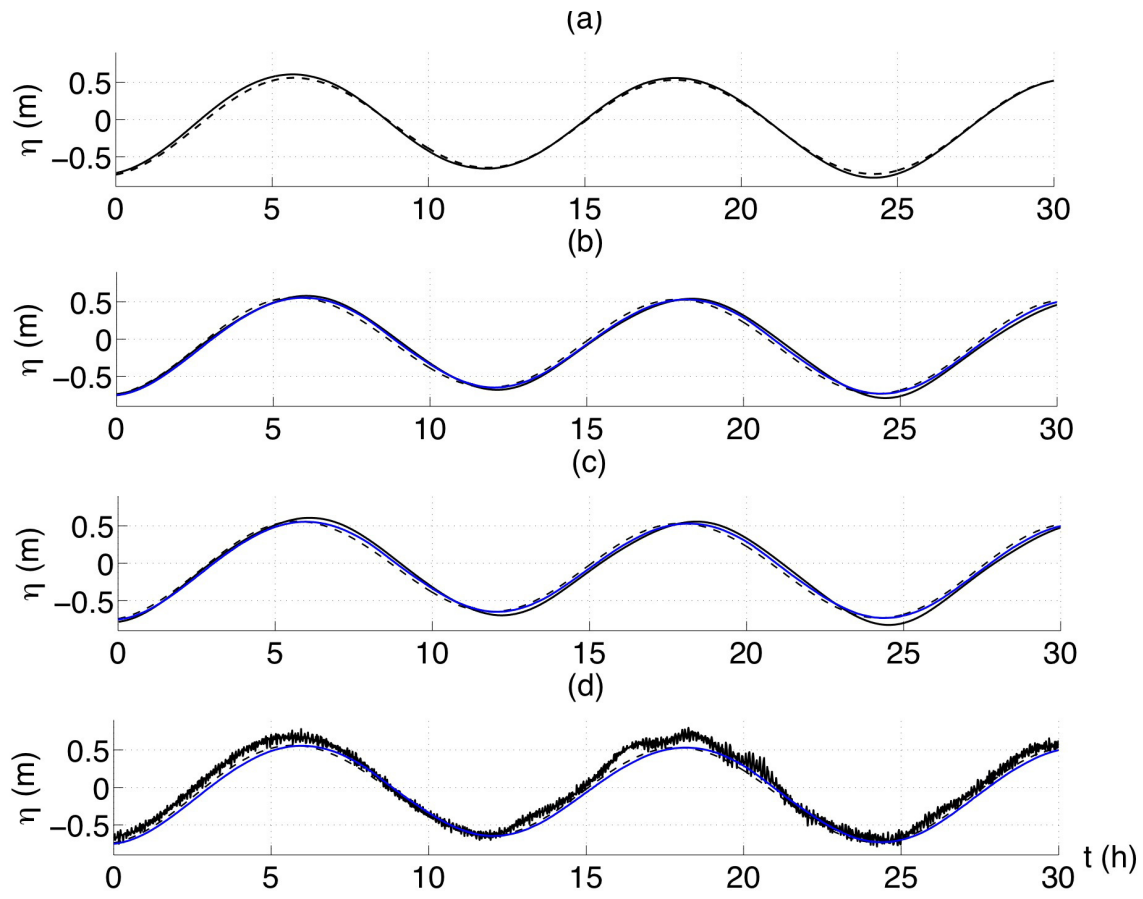


Figure 26: Tide only simulations. Measured tide surface elevations (solid line), compared to FUNWAVE-TVDs 40 meter grid results (dashed line) and 10 meter grid results (blue solid line), at four locations: (a) A Beacon, (b) Tug Berth, (c) Sulfur Point, (d) Moturiki.

and 10 m grids, at the: (a) A Beacon (only in 40 m grid), (b) Tug Berth, (c) Sulfur Point, (d) Moturiki locations, compared to the measured tide surface elevations (obtained by filtering actual data). We see a good agreement between these, and only little differences between the 40 m and 10 m grid results.

5.3.5 Results: Tide plus tsunami simulations

Converged boundary conditions, both elevation and current components, used in the tsunami only simulations were linearly added to the similarly converged boundary conditions used in the tide only simulation along the 40 m grid offshore boundary (Fig. 23c). The combined surface elevations and velocities were used to drive the simulations of tide and tsunami together. Time series of surface elevation and current at stations located along the boundary of the 10 meter grid were computed in the 40 m resolution grid results, and used to force the 10 meter grid model. The latter results were compared to the 40 m grid result to assess convergence, and improve resolution in the area of interest.

Fig. 27 shows surface elevations computed in the tide-tsunami simulations, in the 40 m grids, at the: (a) A Beacon, (b) Tug Berth, (c) Sulfur Point locations, compared to the measured surface elevations, as well as to the linear superposition of tsunami and tide only simulations in the same grid. We see a better agreement of the measured data with the combined tide-tsunami simulations with the and discrepancies between the latter and the linearly superimposed simulations are largest for the larger waves in the tsunami wave train, which may be indicative of nonlinear effects.

Fig. 28 shows the surface elevation computed in the 40 m grid, at the anchor point location of the ADCP buoy (Fig. 21) for the tsunami only, tide only, and tide-tsunami simulations. No data was available for comparison, but we computed the range of variation of the surface elevation in a 40 m radius around the anchor point, which represents the buoy radius of gyration. Only minor change in surface elevation can be seen within this radius. By contrast, Fig. 29, 30 and 31, which show the computed velocity magnitude $|U|$ and components u and v , and measured values, at both the anchor point in the 40 and

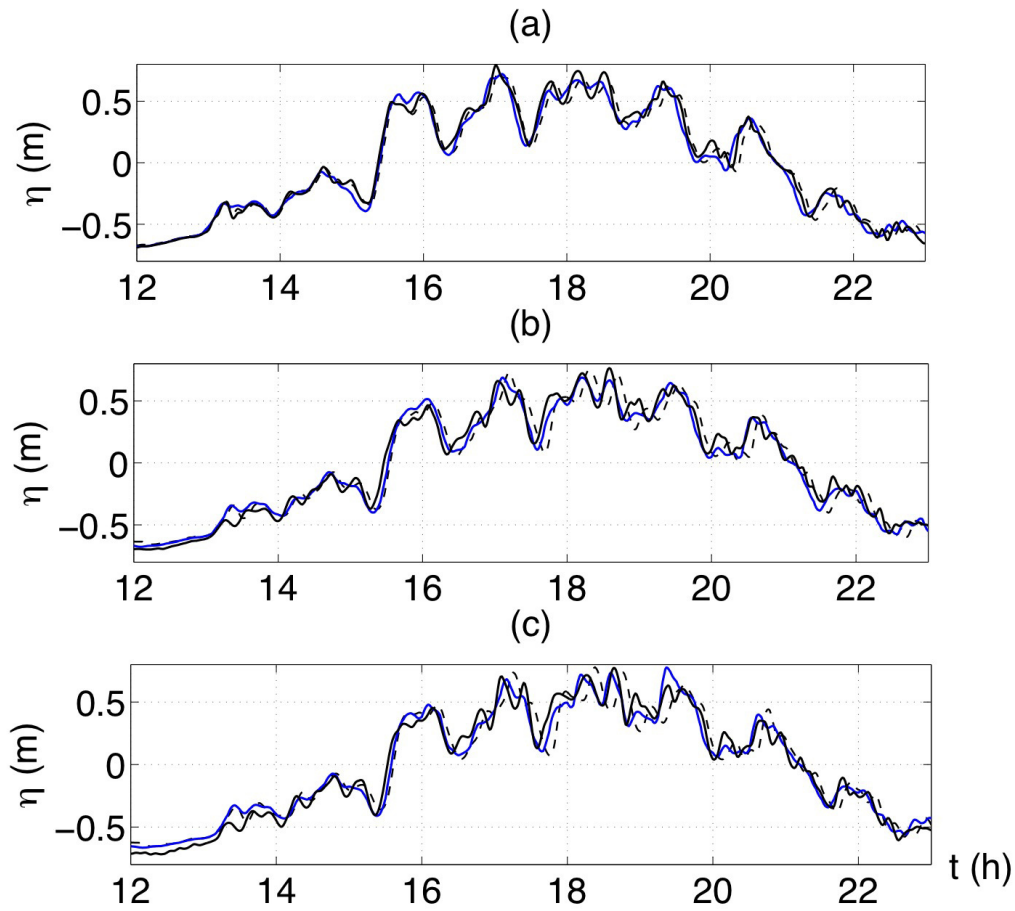


Figure 27: Tide-tsunami simulations. Measured surface elevations (solid line), compared to FUNWAVE-TVDs 40 meter grid results of tide and tsunami alone linearly superimposed (dashed line) and results of simulations using a combined tide-tsunami boundary condition (blue solid line), at three locations: (a) A Beacon, (b) Tug Berth, (c) Sulfur Point.

10 m grids, and within the buoy radius of gyration in the 10 m grid, for the three types of simulations (tsunami only, tide only, and tide-tsunami), shows significant variations in velocity near the anchor point. Because the ADCP moved during measurements, it is not clear where within this area the buoy was located and hence one should compare data to model results within the radius of gyration area. When doing this, we see a good agreement of measured velocity magnitude with those predicted in the 10 m grid in all three cases. The agreement is also good for the u-component of velocity in all three cases, but for the v-component, while the magnitude is reasonable, there seems to be a sign change in the tsunami only simulations and for the tide only simulations, some higher-harmonics seem to be missing. The latter could be related to an insufficiently accurate modeling of bottom friction. However, for the combined tide-tsunami simulations, the agreement with measurements seems better, which could indicate problems in isolating the tsunami and tide currents from the combined measurements.

5.4 Benchmark Test 4: Seaside, Oregon

In this test, a single long-period wave propagates into a combination of linear slopes and onto a model of the town of Seaside, Oregon. Throughout the experiment, measurements of free surface, velocity and momentum flux were recorded in several locations inside the tank. The bathymetry data is available with 1 cm resolution in both directions (Figure 32). The water depth at the wave-maker location is 0.97m. The generated wave is a custom wave meant to maximize the stroke of the wave-maker, and it is not a solitary wave. Four offshore gauges as well as 31 onshore gauges were located in several locations. Figure 33 shows the location of onshore gauges. The purpose of this study is to provide a comparison

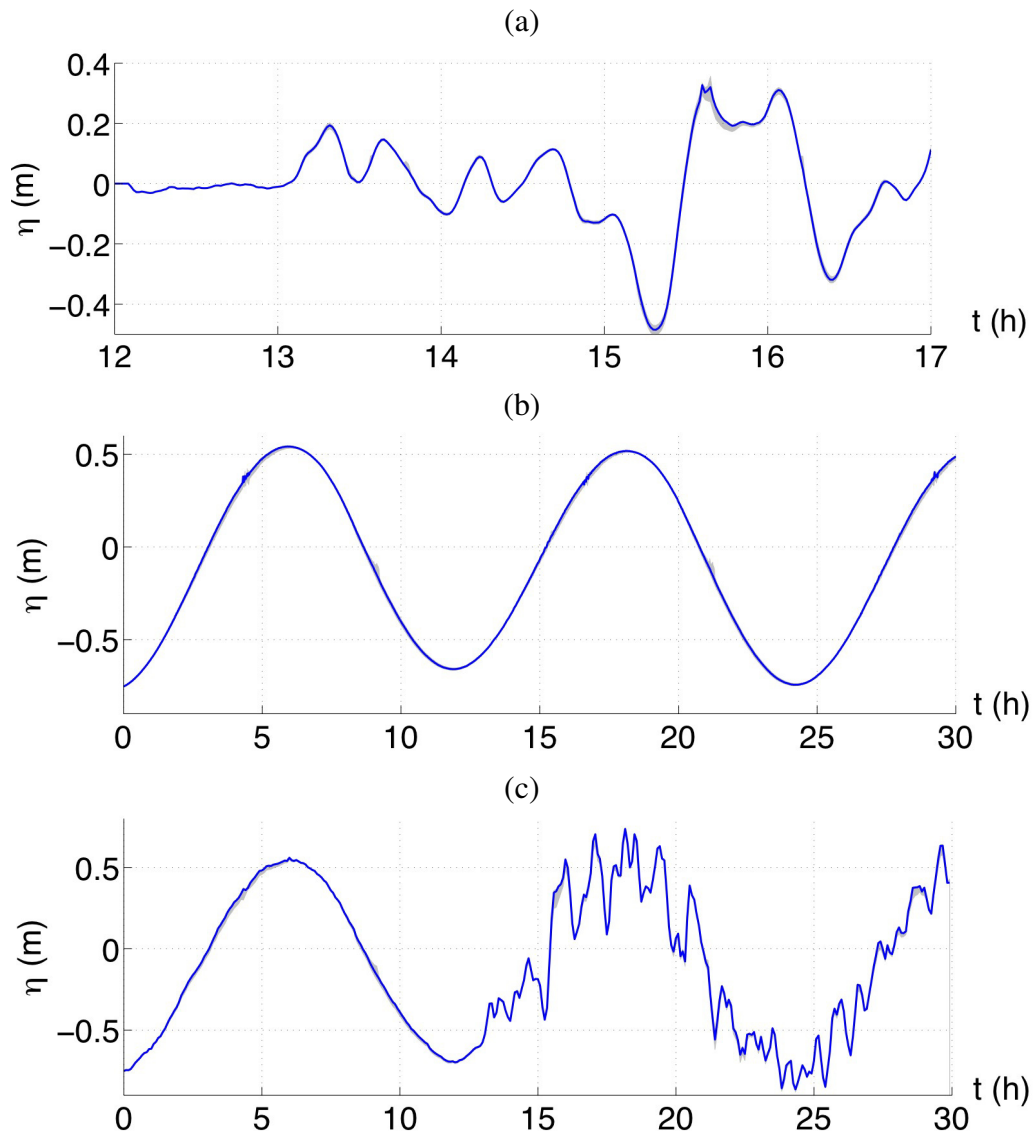


Figure 28: Surface elevations predicted by FUNWAVE-TVD in the 40 meter (solid blue line) and 10 meter (black dashed line) grid, at the ADCP buoy location (Fig. 21), in: (a) tide only, (b) tsunami only; and (c) tide-tsunami simulations. The shaded region represents the range of surface elevations predicted within the buoy 40 m radius of gyration.

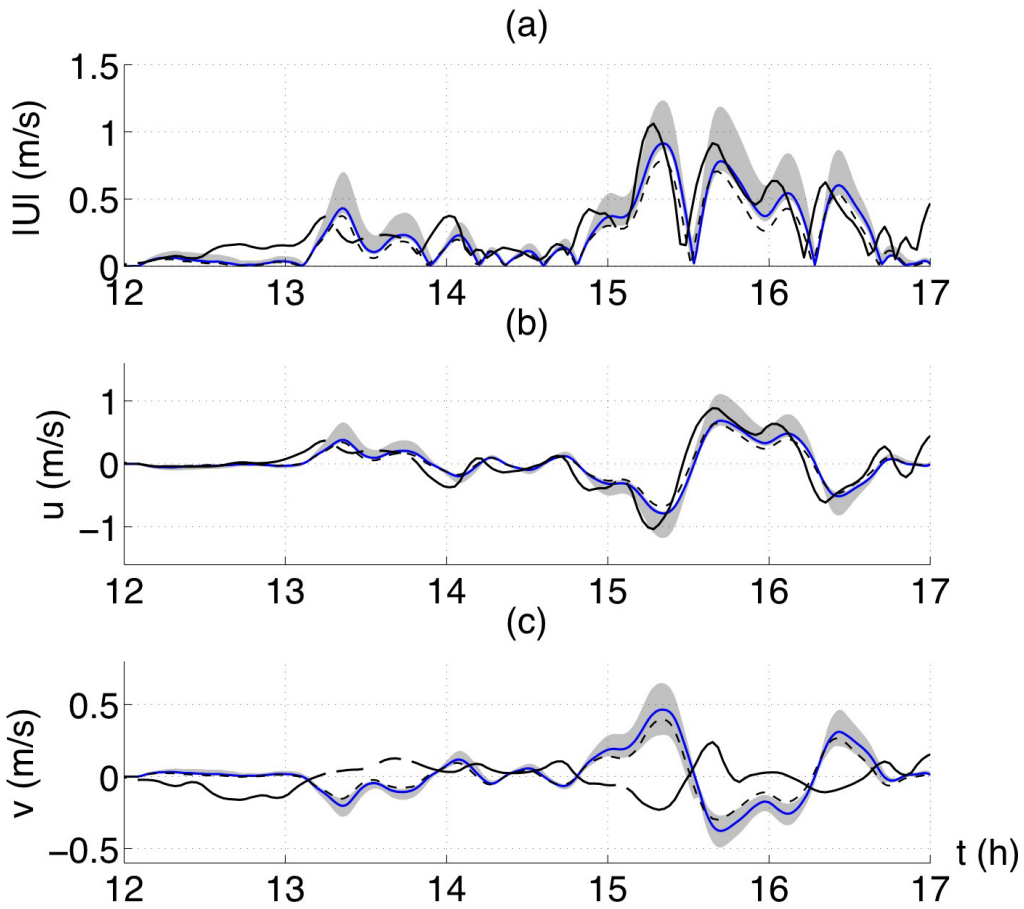


Figure 29: Tsunami only simulations. Measured tsunami current magnitude $|U|$ and velocity components, u and v at the ADCP buoy (solid line), detided and compared to FUNWAVE-TVDs 40 meter grid results (dashed line) and 10 meter grid results (blue solid line). The shaded region represents the range of values predicted in the 10 m grid, within the buoy 40 m radius of giration.

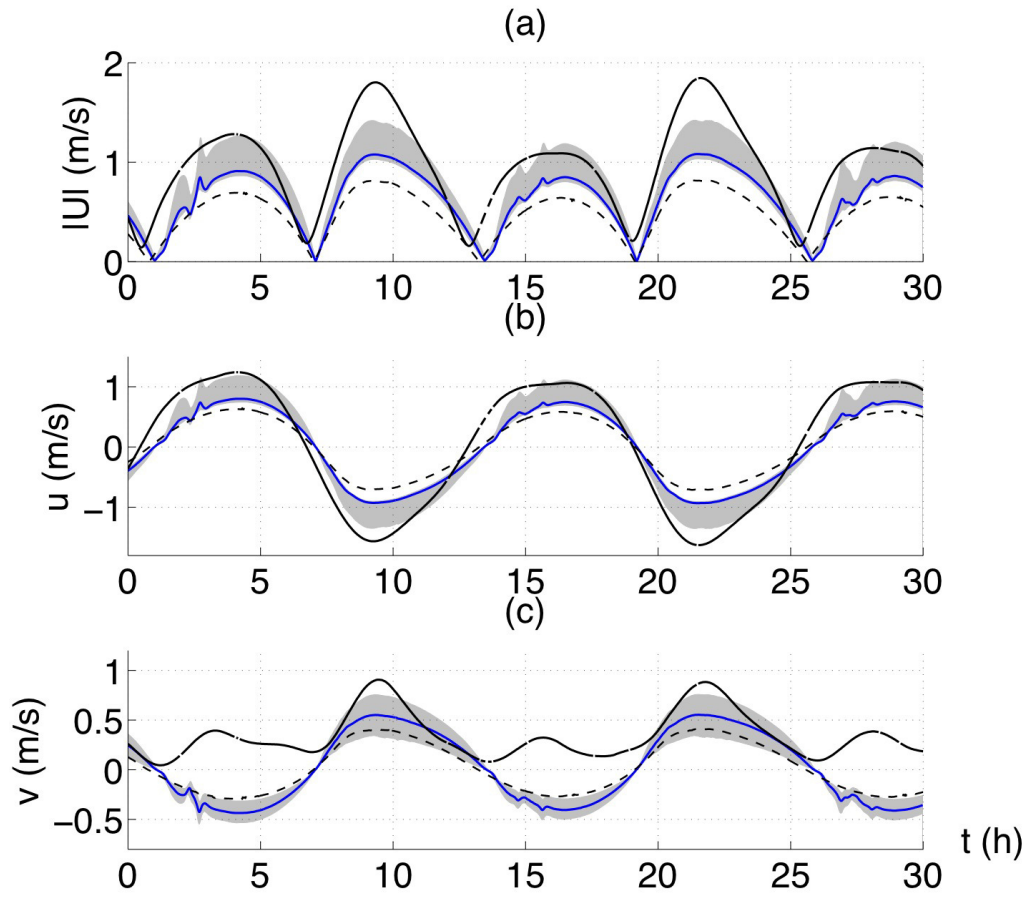


Figure 30: Tide only simulations. Measured tide current magnitude $|U|$ and velocity components, u and v at the ADCP buoy (solid line), compared to FUNWAVE-TVDs 40 meter grid results (dashed line) and 10 meter grid results (blue solid line). The shaded region represents the range of values predicted in the 10 m grid, within the buoy 40 m radius of giration.

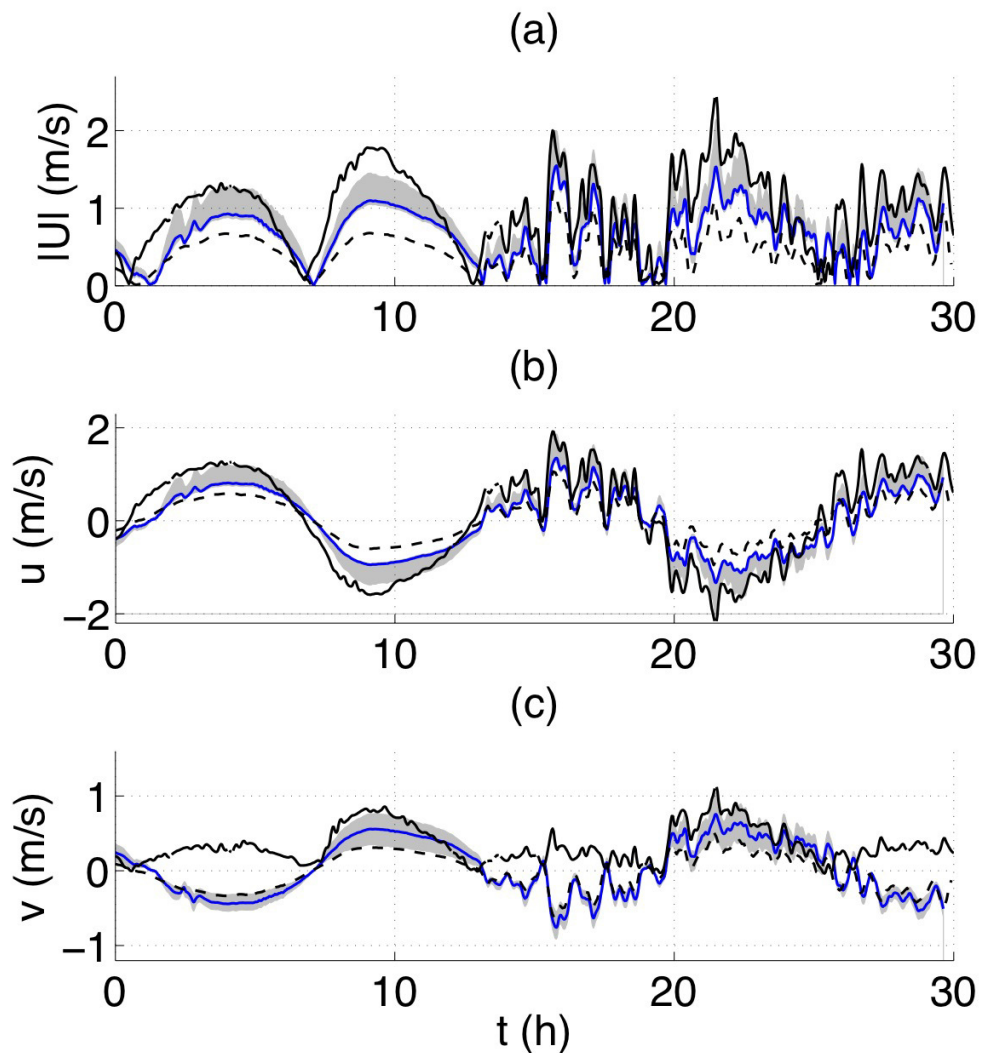


Figure 31: The complete velocity signal (tide and tsunami) measured at the ADCP buoy are represented with the solid line. The dashed line indicates FUNWAVE-TVD output at the anchor point location, and the shaded region indicates the maximum and minimum values within 40 meters of the anchor point. The magnitude of the velocity is shown in (a). The u and v components of the velocity are aligned with the orientation of the simulation grids, and are shown in (b) and (c). Time is measured in hours after the earthquake.

between measured flow depth data, velocity, and momentum flux for gauges B1, B4, B6, and B9 shown in Figure 33.

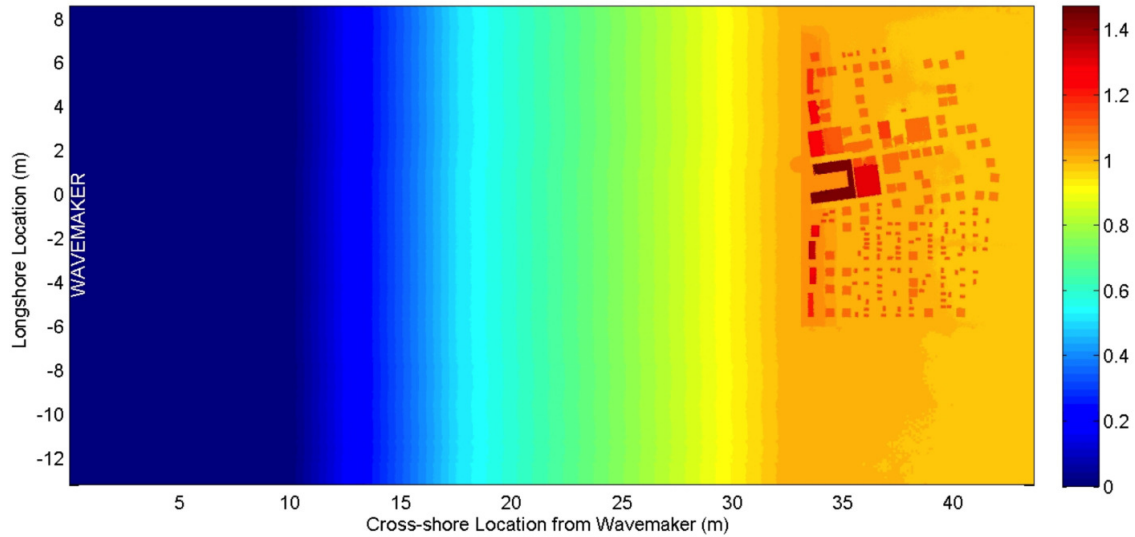


Figure 32: The Bathymetry Data.

5.4.1 Model Setup

Eight different runs were performed (Table 3). These runs were performed for three purposes. First, runs 1-5 were performed to investigate the effects of various friction values (Section 3.1). Runs 1-5 were conducted using a uniform grid size of 5 cm. After post-processing, it was observed that the value of 0.001 for C_d generated the best results, confirming the suggestion of Park et al. (2013).

Runs 6-9 were conducted to study the convergence of the model (Section 3.2). Convergence tests used uniform grid spacings of 10, 8, 4 and 3 cm resolution, using the same friction factor as run 2 to provide the comparison for the chosen C_d . It was found that the

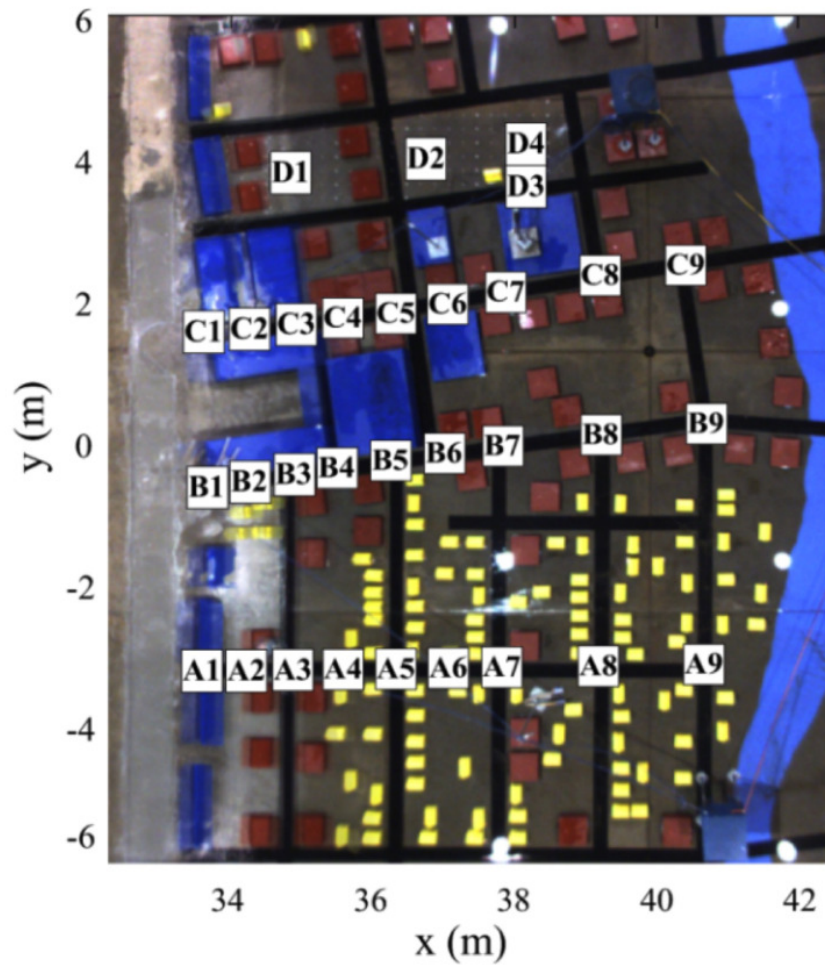


Figure 33: Location of gauges.

Runs	Grid Size(cm)	C_d	Bathymetry
1	5.0	0.0	Original
2	5.0	0.001	Original
3	5.0	0.0025	Original
4	5.0	0.005	Original
5	5.0	0.010	Original
6	10.0	0.001	Original
7	8.0	0.001	Original
8	4.0	0.001	Original
9	3.0	0.001	Original
10	5.0	0.001	Smoothed

Table 3: Different runs performed for this benchmark.

model converges for the grid size 5 cm and smaller. Thus, the 5 cm grid size was chosen to perform the main run for this benchmark.

Park et al. (2013) have claimed that for the stability of their model, they had to smooth the bathymetry in a way that the largest slope was 2:1 in their setup. This means that the sides of the buildings in their model setup were a slope of 2:1 and not a vertical straight line (or, more precisely, a change in elevation over one grid space). Although FUNWAVE-TVD did not need any topography smoothing to run stably, we investigated the difference associated with smoothing by repeating run 2 with smoothed topography to observe the differences between the two conditions (run 10).

The initial wave condition was generated using the coupling capability of FUNWAVE-TVD. The water surface elevation recorded close to the wave-maker was used to derive a stationary input wave boundary condition at $x=0.0\text{m}$ in the domain (Figure 33). Also, sponge layer (20 cm wide) was located on the right side of the domain to avoid reflection

effects.

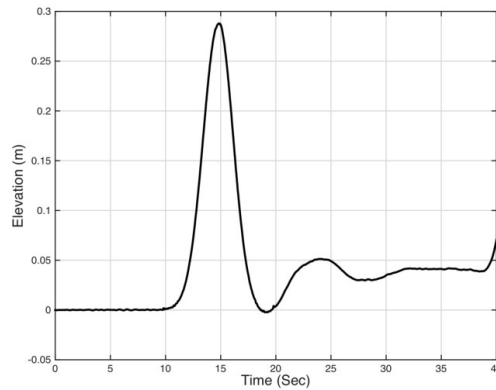


Figure 34: Water surface in the left part of the domain obtained from recorded data.

5.4.2 Results

The effect of varying drag coefficient C_d

Figures 35-38 demonstrate the comparison for the runs 1-5 that were performed with 5 different values. As shown in these figures, the results for $C_d = 0.001$ are similar to the results Park et al. (2013) achieved, and provides the best fit to the measured data. This conclusion was achieved using a mean square error analysis. Also, the arrival time of the wave to the gauges far from the shoreline (e.g. B9) confirms the fact that the value of $C_d=0.001$ is the best choice to be used here. The black solid line in Figures 4-?? depicts the simulation results for $C_d = 0.0$. It is clear through looking at the velocity values for gauges further onshore (B6 and B9) that zero friction does not produce a reasonable fit for velocity and momentum flux values. The thinner lines in Figures 35-38 show the modeling results for drag coefficient larger than 0.001. For these values the flow is over-dissipated. For example, looking at the momentum flux values for the gauge B1 show the dissipative

behavior of the flow in comparison to real condition. Therefore, as also suggested by Park et al. (2013), the value for C_d is chosen to be 0.001 for the other tests performed for the study.

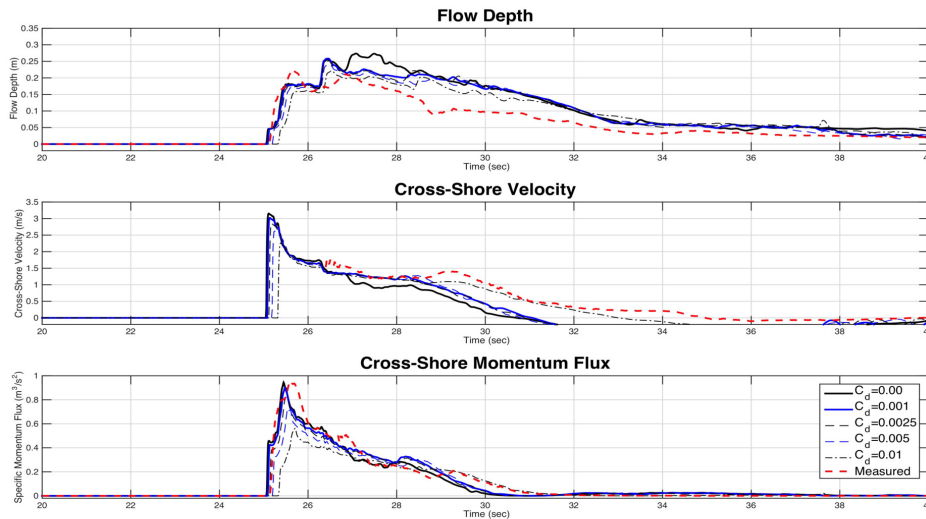


Figure 35: Comparison between 5 different friction values for B1.

5.4.3 Convergence

In order check model convergence, runs 6-9 (Table 1) were conducted with four different resolutions, two of them coarser than previous runs (Runs 6 and 7), and two of them finer (Runs 8 and 9). Figure 39 shows the comparison of cross-shore velocity for these four runs with the original 5 cm grid size run at B1. The results improve significantly for finer resolutions runs in comparison to 8 and 10 cm runs. However, for grid sizes smaller than 5cm, the results converge, and minor difference between the calculated results are probably the consequence of gauge locating errors, which is inevitable since grid points

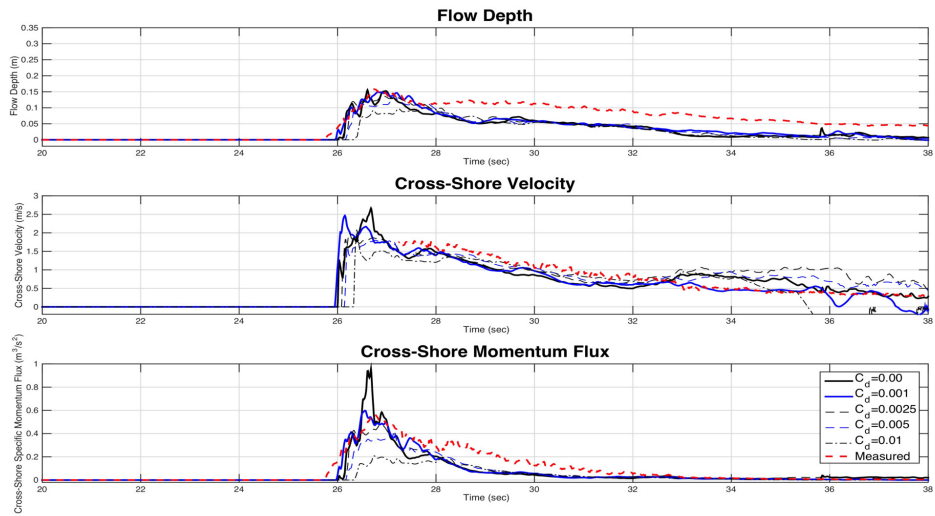


Figure 36: Comparison between 5 different friction values for B4.

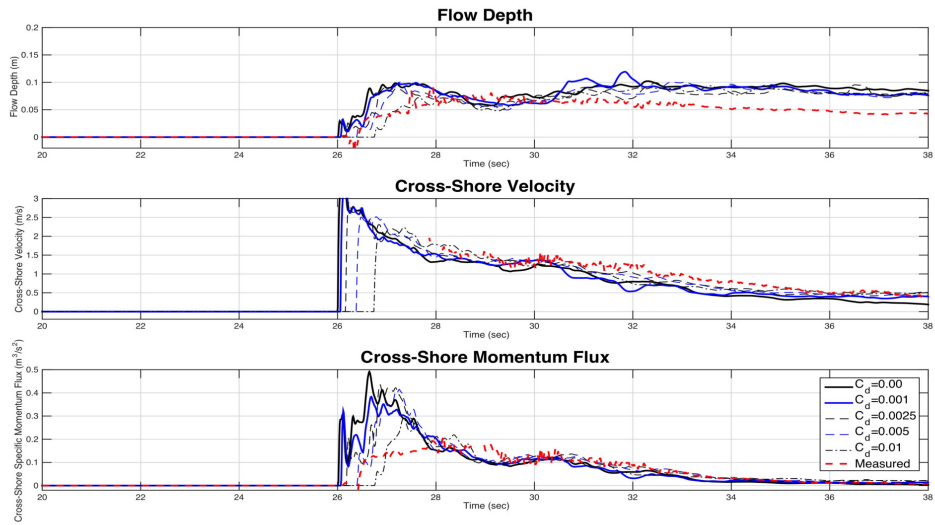


Figure 37: Comparison between 5 different friction values for B6.

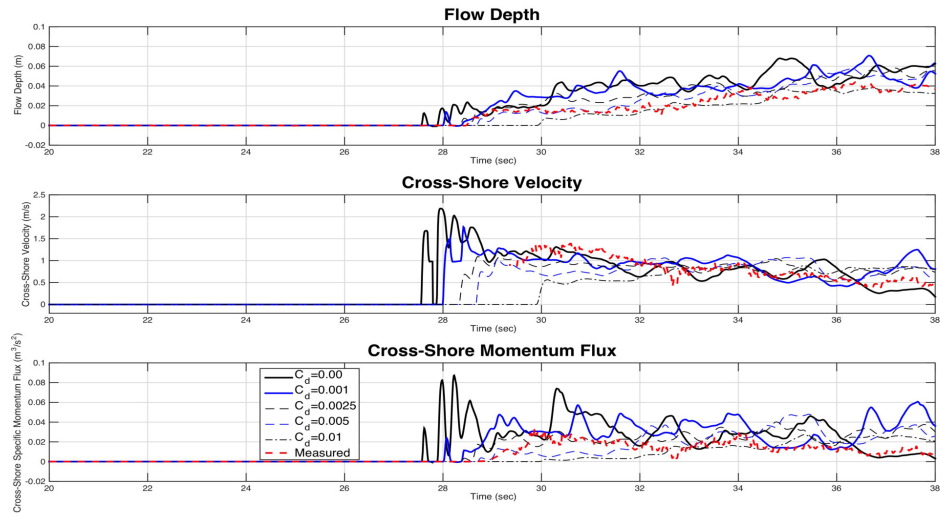


Figure 38: Comparison between 5 different friction values for B9.

will not fall on top of each other for 5, 4 and 3 cm resolution grids. We could have avoided this problem by simulating with a 2.5 cm sized grid, but the original data has the resolution of 1 cm that will force interpolation of data in between the points.

5.4.4 The effect of bathymetry smoothing

Park et al. claimed that for stability of their model they had to smooth the bathymetry around the structures. Although, as mentioned before FUNWAVE-TVD can be implemented without such manipulation, run 10 was performed to investigate the differences between two conditions. The maximum bottom slope in the domain was controlled by the grid resolution, and any slope that larger than 2:1 was smoothed until it was no longer this steep. Thus, for the run 10 all of the vertical walls were smoothed until the sidewalls of the

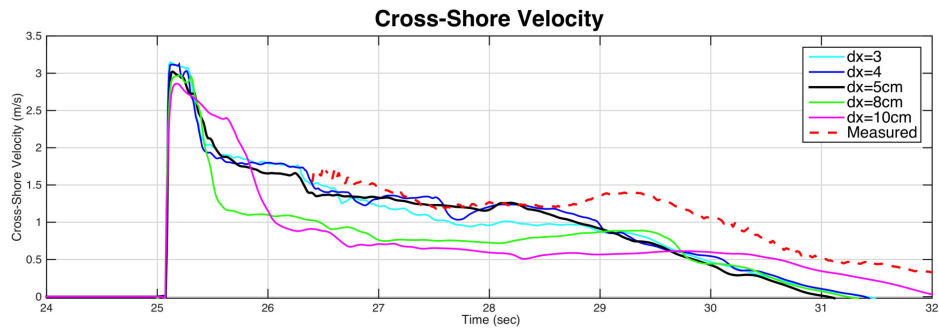


Figure 39: Comparison between calculated cross-shore velocity for 5 different grid sizes at B1.

structures had the slope of 2:1. This process resulted in smaller surfaces for the top of the building in smoothed condition. Figure ?? shows a difference plot between two conditions for the area close to the U-shape structure next to gauges B and C. Figure 41 shows a 3D view of two different bathymetry conditions (original and smoothed). By looking at the U-shape structure in the middle of the domain, one can observe the differences between two bathymetries.

Figures 42-45 shows the comparison between two different bathymetry conditions for the four gauges mentioned before. The simulated results for the cross-shore velocity in smoothed condition shows better agreement in the interval between 28-32 seconds. The observed drop in the velocity values is most probably because of the volume of the water that was left on top of the structures during the inundation process poured back into the domain, resulting in an artificial increase in water surface elevations, and also decreasing the velocity values. The reason that smoothed condition shows better agreement is that the surfaces above the structures are smaller in smoothed condition, and less amount of

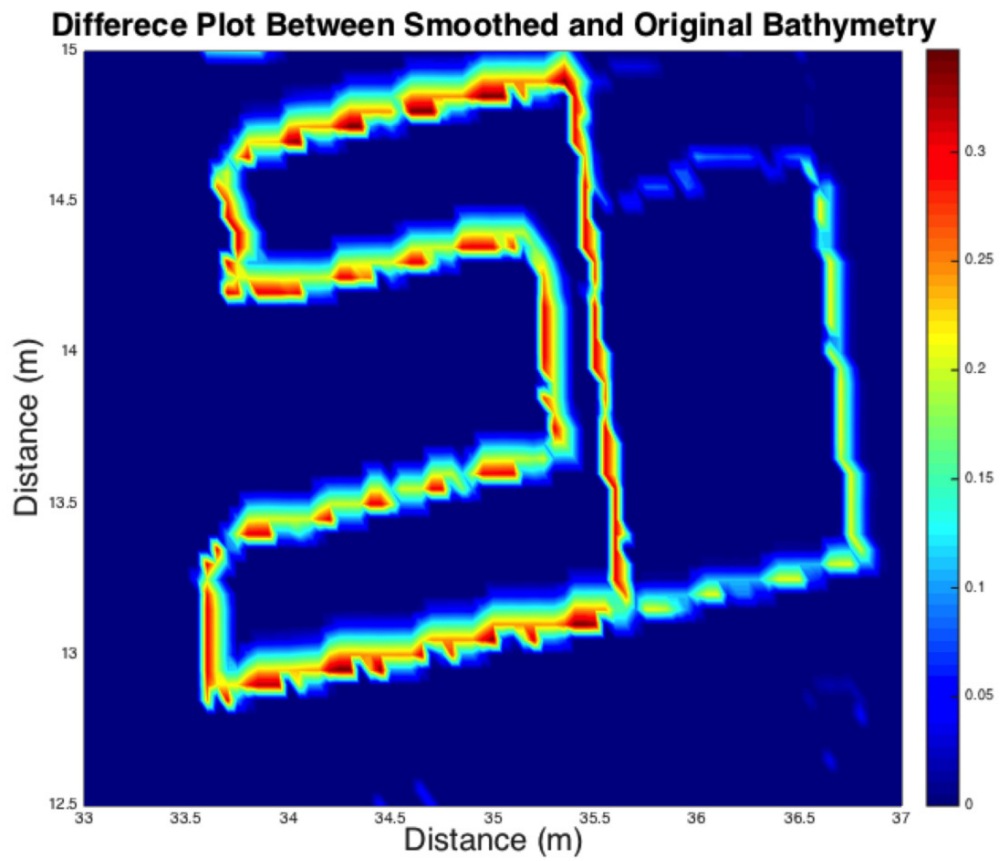


Figure 40: Difference plot between the smoothed and original bathymetry close to the U-shape structure next to B1 and B4.

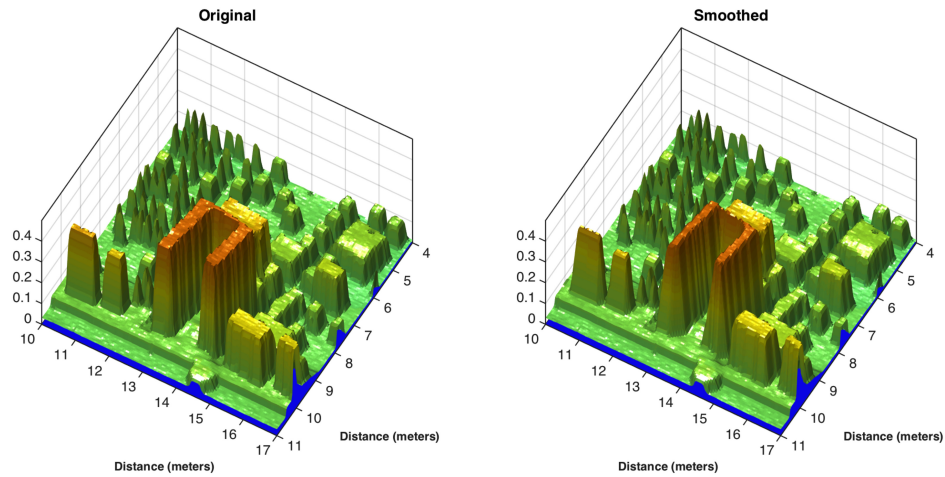


Figure 41: The figure on the left shows the original onshore bathymetry used in runs 1-9, and the figure on the right shows the smoothed bathymetry used in run 10.

water are captured on top of the buildings during inundation. Also, simulation results for the A gauges shows better agreement with measured data in comparison to B and C gauges. This is probably because the B and C gauges are next to the largest building in the domain (U-shaped structure), and A gauges are next to much smaller buildings. Thus, close to A gauges less amount of water will pour back into the domain after the buildings are inundated, so the water surface and velocity evaluations looks better.

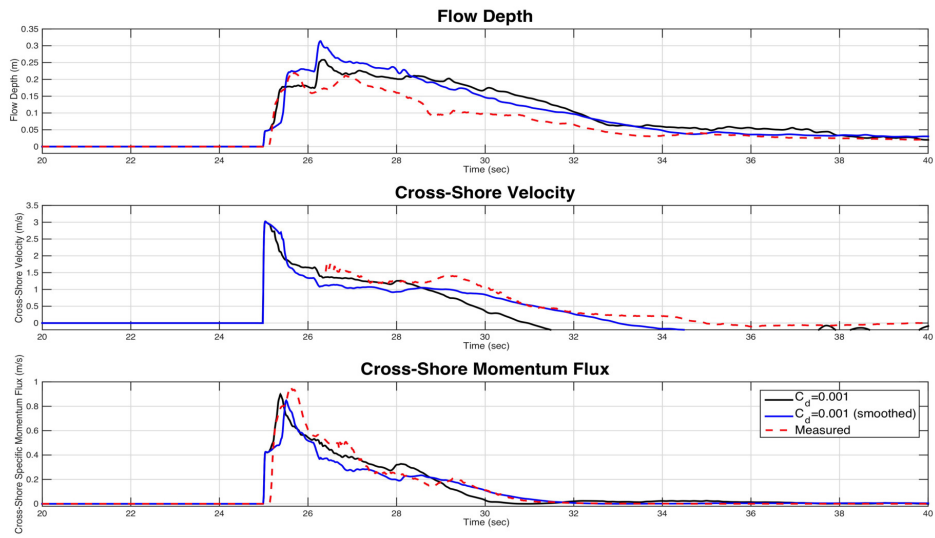


Figure 42: Comparison between original and smoothed bathymetry for B1.

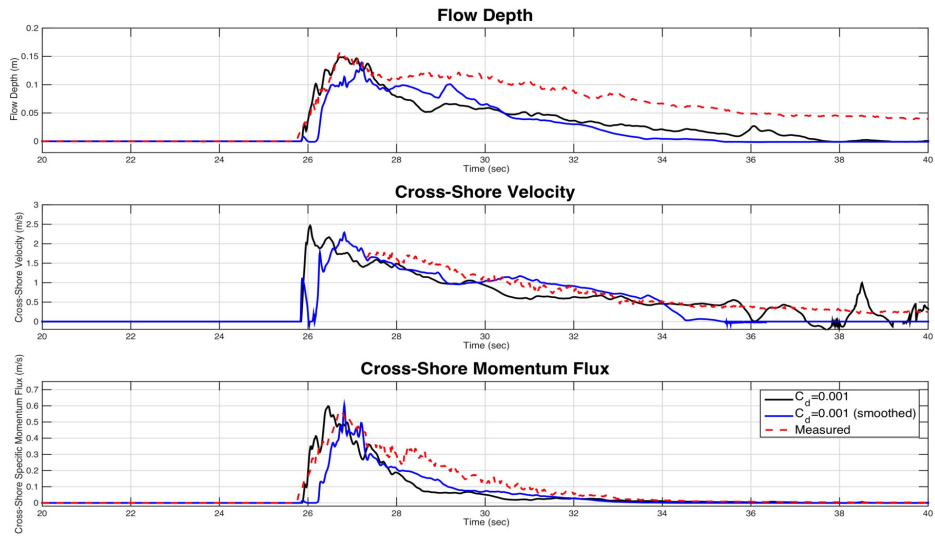


Figure 43: Comparison between original and smoothed bathymetry for B4.

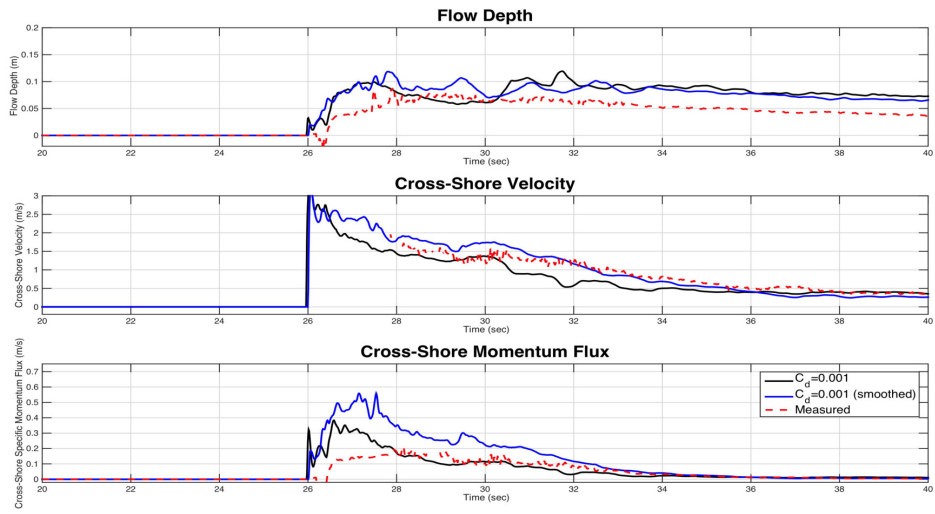


Figure 44: Comparison between original and smoothed bathymetry for B6.

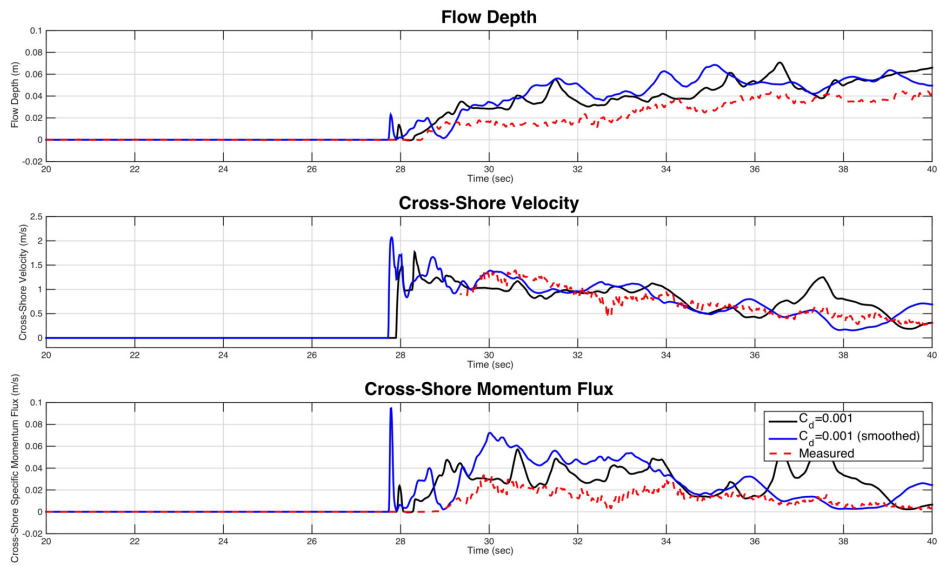


Figure 45: Comparison between original and smoothed bathymetry for B9.

5.5 Solitary Wave Propagation over a Complex Shelf

For FUNWAVE-TVD, the model bathymetry was constructed by extending the bathymetry data to the left by 8.76 m (100 grid points in the model grid) with a constant water depth of 0.78 m in order to initialize the solitary wave on the left side. Grid convergence test was conducted using two grid resolutions. The test indicated that the reduction of grid size from (0.0876m, 0.1063m) (dx,dy) to (0.0438m, 0.0532m) did not affect the model results. The simulations were performed using two wave breaking schemes implemented in FUNWAVE-TVD: the natural TVD shock capturing scheme (SWE breaker) implemented in Shi et al., (2012), and the artificial eddy-viscosity breaker (VIS breaker) developed by Kennedy et al. (2000).

Figure 48 shows time series of surface elevation modeled by the SWE breaker model and the VIS breaker model with comparison to the measurements at Gauge 1-9 (from top to bottom). Both models predicted well the solitary wave propagation and its reflection from the shore. The models also captured the collision of edge waves propagating around the two sides of the island, as indicated at the gauge behind the island (Gauge 3). The comparisons between the SWE breaker model and VIS breaker model show that the surface elevations predicted by the two models are generally identical. Figure 49 shows model/data comparisons of velocity components (u, v) at the ADV 1. Both models predicted the peak velocity and the entire trend of velocity variation in time at the measurement location. Again, the results from the two models are basically identical except slight differences in later time when wave breaking is involved.

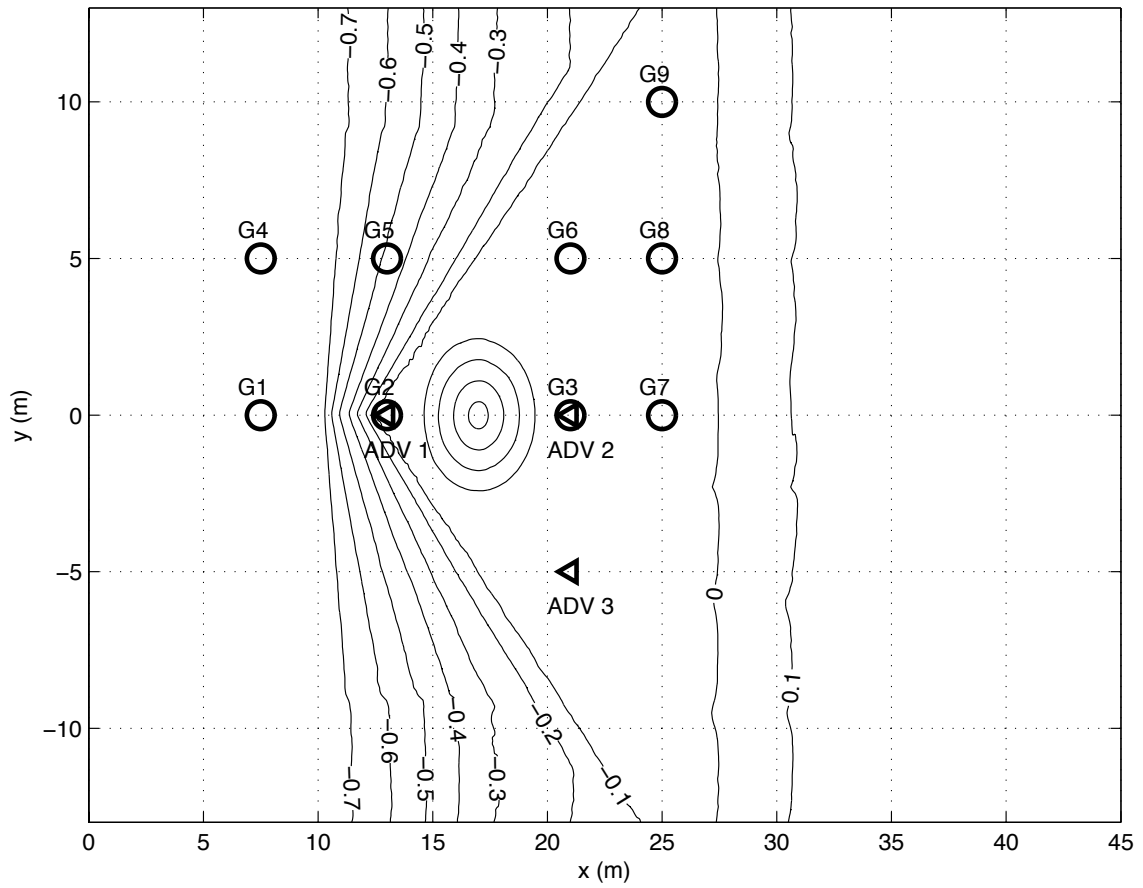


Figure 46: Basin geometry and gauge locations. Experiment of Swigler (2009).

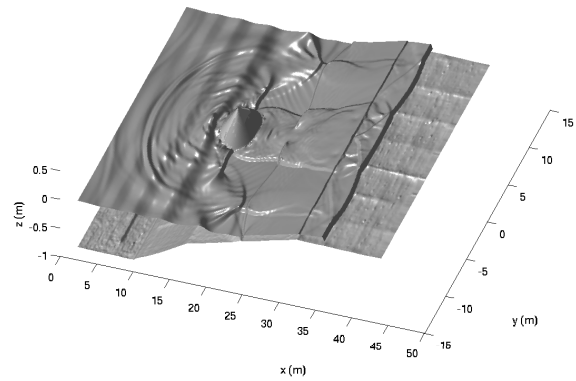
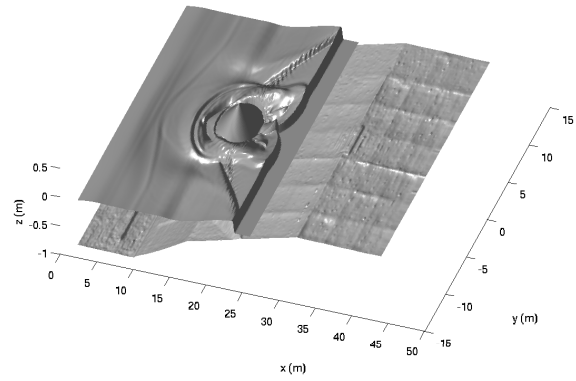
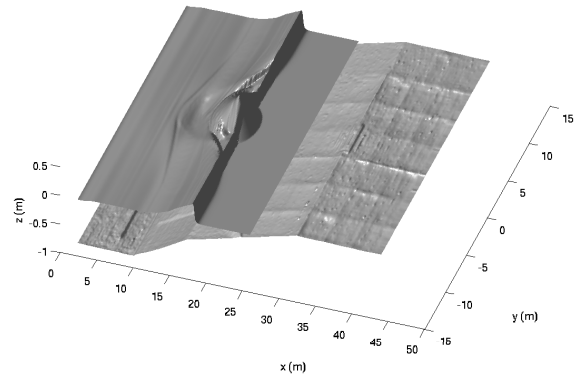


Figure 47: Simulated solitary wave run-up on model bathymetry (after Shi et al., 2012).

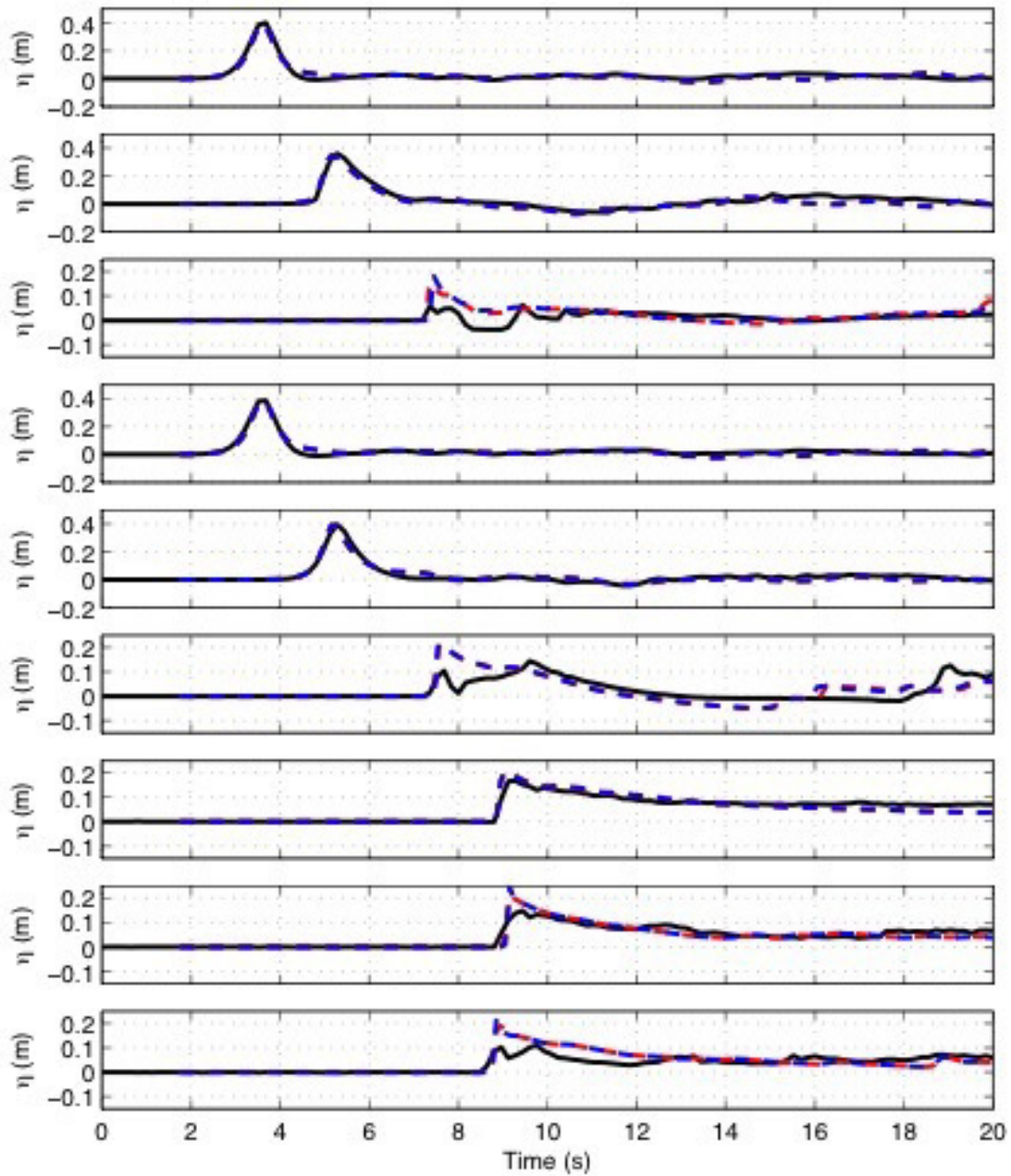


Figure 48: Model/data comparisons of time series of surface elevation at Gauge 1-Gauge9 (from top to bottom). Solid line: data, red dashed line: VIS breaker model, blue dashed line: SWE breaker model.

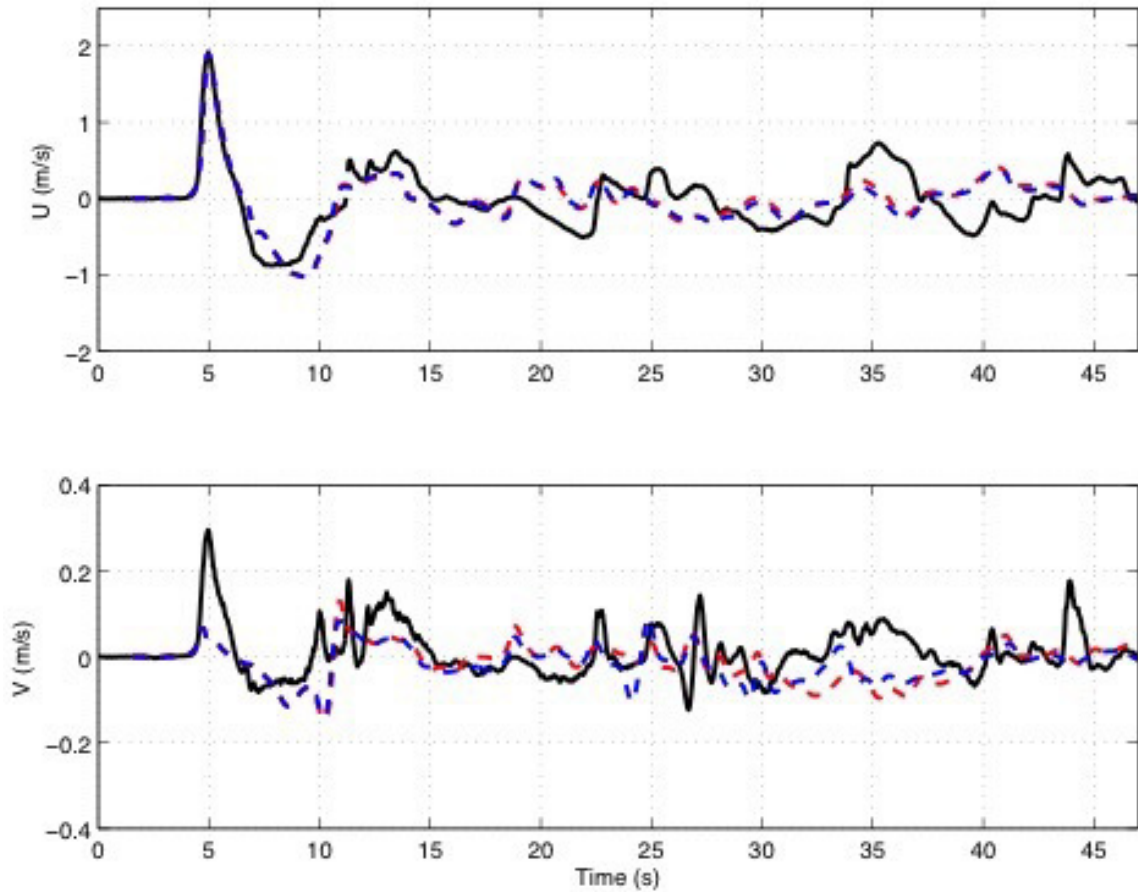


Figure 49: Model/data comparisons of time series of velocity components (u,v) at ADV 1. Solid line: data, red dashed line: VIS breaker model, blue dashed line: SWE breaker model.

References

- Borrero, J., Bell, R., Csato, C., DeLange, W., Greer, D., Goring, D., Pickett, V. and Power, W., 2012, "Observations, effects and real time assessment of the March 11, 2011 Tohoku-oki tsunami in New Zealand", *Pure and Applied Geophysics*, **170**, 12291248, doi:10.1007/s00024-012-0492-6.
- Chen, Q., Kirby, J. T., Dalrymple, R. A., Kennedy, A. B. and Chawla, A., 2000, "Boussinesq modeling of wave transformation, breaking and runup. II: Two horizontal dimensions", *Journal of Waterway, Port, Coastal and Ocean Engineering*, **126**, 48-56.
- Chen, Q., 2006, "Fully nonlinear Boussinesq-type equations for waves and currents over porous beds." *Journal of Engineering Mechanics*, **132**, 220-230.
- Cheung, K F, Bai, Y. and Yamazaki Y., 2013, "Surges around the Hawaiian Islands from the 2011 Tohoku tsunami", *J. Geophys Res.: Oceans*, **118**, 5703-5719, doi:10.1002/jgrc.20413.
- Gottlieb, S., Shu, C.-W., Tadmor, E., 2001, "Strong stability-preserving high-order time discretization methods." *SIAM Review*, **43** (1), 89-112.
- Grilli, S.T., Harris, J. C., Tajalli Bakhsh, T., Masterlark, T. L., Kyriakopoulos, C., Kirby, J. T. and Shi, F., 2013, "Numerical simulation of the 2011 Tohoku tsunami based on a new transient FEM co-seismic source: Comparison to far- and near-field observations", *Pure and Applied Geophysics*, **170**, 1333-1359, doi:10.1007/s00024-012-0528-y.
- Grilli, S. T., O'Reilly, C., Harris, J. C., Tajalli Bakhsh, T., Tehranirad, B., Banihashemi,

- S., Kirby, J. T., Baxter, C. D. P., Eggeling, T., Ma, G. and Shi, F., 2015. "Modeling of SMF tsunami hazard along the upper U. S. East Coast: Detailed impact around Ocean City, MD." *Natural Hazards*, **76**, 705-746, doi: 10.1007/s11069-014-1522-8.
- Kennedy, A.B., Chen, Q., Kirby, J.T., Dalrymple, R.A., 2000. "Boussinesq modeling of wave transformation, breaking and runup. I: 1D." *Journal of Waterway, Port, Coastal and Ocean Engineering*, **126**, 39-47.
- Kennedy, A.B., Kirby, J.T., Chen, Q., Dalrymple, R.A., 2001. "Boussinesq-type equations with improved nonlinear performance." *Wave Motion*, **33**, 225-243.
- Kirby, J. T., Shi, F., Tehranirad, B., Harris, J. C. and Grilli, S. T., 2013. "Dispersive tsunami waves in the ocean: model equations and sensitivity to dispersion and Coriolis effects", *Ocean Modelling*, **62**, 39-55, doi:10.1016/j.ocemod.2012.11.009.
- Lloyd, P. M. and Stansby, P. K., 1997a, "Shallow-water flow around model conical islands of small side slope. II: Submerged", *Journal of Hydraulic Engineering*, **123**(12), 1068-1077.
- Lynett, P. J., Gately, K., Nicolsky, D. and Wilson, R., 2016, "Summary report of the NTHMP Current Modeling Workshop", draft report.
- Lynett, P. J., et al., 2017, Inter-model analysis of tsunami-induced coastal currents, *Ocean Modelling*, under revision.
- Park, H., Cox, D. T., Lynett, P. J., Wiebe, D. M., and Shin, S., 2013. "Tsunami inundation modeling in constructed environments: A physical and numerical comparison of

- free-surface elevation, velocity, and momentum flux”, *Coastal Engineering*, **79**, 9-21.
- Shi, F., Kirby, J. T., Harris, J. C., Geiman, J. D. and Grilli, S. T., 2012. “A high-order adaptive time-stepping TVD solver for Boussinesq modeling of breaking waves and coastal inundation”, *Ocean Modelling*, **43-44**, 36-51.
- Swigler, D. T., 2009, “Laboratory study investigating the three-dimensional turbulence and kinematic properties associated with a breaking solitary wave”, M.S. thesis, Ocean Engineering, Texas A&M University.
- Tappin D.R., Grilli S.T., Harris J.C., Geller R.J., Masterlark T., Kirby J.T., Shi, F., Ma, G., Thingbaijam, K. K. S. and Maig, P. M., 2014, “Did a submarine landslide contribute to the 2011 Tohoku tsunami ?” *Marine Geology*, **357**, 344-361, doi: 10.1016/j.margeo.2014.09.043.
- Tehrani-rad, B., Shi, F., Kirby, J.T., Harris, J.C., Grilli, S., 2011. “Tsunami benchmark results for fully nonlinear Boussinesq wave model FUNWAVE-TVD, Version 1.0”. Research Report No. CACR-11-02, Center for Applied Coastal Research, University of Delaware.
- Tehrani-rad B., Harris, J.C., Grilli, A.R., Grilli, S.T., Abadie, S., Kirby, J.T. and Shi, F., 2015, “Far-field tsunami impact in the north Atlantic basin from large scale flank collapses of the Cumbre Vieja volcano, La Palma.” *Pure and Applied Geophysics*, **172**(12), 3,589-3,616, doi:10.1007/s00024-015-1135-5.
- Tonelli, M., Petti, M., 2009. “Hybrid finite volume-finite difference scheme for 2DH

- improved Boussinesq equations.” *Coastal Engineering*, **56**, 609-620.
- Tonelli, M., Petti, M., 2010. “Finite volume scheme for the solution of 2D extended Boussinesq equations in the surf zone.” *Ocean Engineering*, **37**, 567-582.
- Toro, E.F., 2009. *Riemann solvers and numerical methods for fluid dynamics: a practical introduction*, third edition. Springer, New York.
- Wei, G., Kirby, J.T., Grilli, S.T., Subramanya, R., 1995. “A fully nonlinear Boussinesq model for surface waves: Part I. Highly nonlinear unsteady waves.” *Journal of Fluid Mechanics*, **294**, 71-92.
- Yamamoto, S., Daiguji, H., 1993. Higher-order-accurate upwind schemes for solving the compressible Euler and NavierStokes equations”, *Computers and Fluids*, **22**, 259-270.
- Yamamoto, S., Kano, S., Daiguji, H., 1998. “An efficient CFD approach for simulating unsteady hypersonic shock-shock interference flows.” *Computers and Fluids*, **27**, 571-580.
- Zhou, J.G., Causon, D.M., Mingham, C.G., Ingram, D.M., 2001. “The surface gradient method for the treatment of source terms in the shallow-water equations.” *Journal of Computational Physics*, **168**, 1-25.